Remote Sensing of Environment 329 (2025) 114910

Contents lists available at ScienceDirect

Remote Sensing of Environment

journal homepage: www.elsevier.com/locate/rse

Discrepancies between time-based and real depth profiles in ocean lidar due to multiple scattering

Mingjia Shangguan *, Yirui Guo, Zhuoyang Liao, Zhongping Lee

State Key Laboratory of Marine Environmental Science, College of Ocean and Earth Sciences, Xiamen University, Xiamen, Fujian 361102, China

ARTICLE INFO

Editor: Menghua Wang

Keywords:
Ocean remote sensing
Lidar
Monte Carlo
Multiple scattering

ABSTRACT

Due to its ability to provide day-and-night profiling and high depth resolution, ocean lidar has become an important tool for marine remote sensing. However, a lidar system provides time-based measurements of backscattered photons, where the distance (or depth for vertical profiling) is a product of light speed in water and the time photons pass. When there are significant contributions of multiple scattering in the backscattered signals of ocean lidar, the perceived depth of these measured photons will be deeper than the real depth. Therefore, if the objective of a lidar system is to sense the vertical profile of particles, the present time-based depth profile will not match the real depth profile of particles in the water column. To address this discrepancy, we carried out semi-analytical Monte Carlo simulations for a wide range of water properties (represented by scattering coefficient, b), focusing on Case-1 water, with platforms including spaceborne, airborne, shipborne, and underwater. In the simulation process, it is assumed that the water column is vertically homogeneous, and the influence of sea surface fluctuations is ignored. Based on the simulated data, relationships between the discrepancy and b, as well as the radius of the received footprint on the water surface (r_s), are established. Sensitivity analysis indicates that the discrepancy is more sensitive to b than to r_s. Further, the impact of the absorption coefficient, scattering phase function, rough sea surface, and vertically non-uniform inherent optical properties on this discrepancy is discussed. Our results not only highlight the significance of considering multiple scattering, particularly for airborne and spaceborne platforms, in sensing the vertical profiles of particles but also provide guidance for interpreting backscattered signals in ocean lidar applications.

1. Introduction

The ocean plays an indispensable role in the global ecosystem, not only regulating climate and maintaining biodiversity but also a crucial part in global biogeochemical processes such as the carbon and mercury cycles (Mason and Sheu, 2002). Therefore, ocean observation data is essential for conducting marine research and predicting ocean changes (Adkins, 2013; Barry et al., 2011; Mason and Sheu, 2002; Regnier et al., 2022). Due to their wide coverage, long-term data acquisition capabilities and high spatial resolution, satellite remote sensing technologies have been widely employed in marine scientific research (Amani et al., 2022; Rani et al., 2021). Over the past few decades, passive ocean color remote sensing has been employed to derive a variety of ocean parameters, such as chlorophyll-*a* concentration (Chl) and particulate matter, by measuring the water-leaving radiance, providing a sustained synoptic view of the distribution of the bio-optical properties of oceanic waters and biogeochemical parameters (Blondeau-Patissier et al., 2014; Hu, 2009). However, passive ocean color remote sensing lacks profiling capabilities and is constrained by solar illumination, making observations impossible in conditions such as the absence of sunlight or low sun angles (Collister et al., 2024; Joint et al., 2000).

To achieve three-dimensional (3D) ocean observations, active lidar technology has been proposed. It can obtain day-and-night profile information of water parameters by detecting the backscattered signal generated by the interaction between laser beams and molecules/particles in the upper water column (Churnside and Shaw, 2020; Jamet et al., 2019). With advances in laser technology, ocean lidar has been applied to various subjects, including optical properties of water (Collister et al., 2018; Shangguan et al., 2024a; Yuan et al., 2022), ocean temperature and salinity (Bao et al., 2022; Gao et al., 2006; Moisan et al., 2024; Spence et al., 2024; Wang et al., 2023; Yang and Shangguan, 2023; Yu et al., 2014), oil spills (Li et al., 2016; Li et al., 2014; Samberg, 2005; Shangguan et al., 2023c), internal waves (Churnside et al., 2012; Magalhaes et al., 2013), fish schools (Churnside and Hunter, 1996;

* Corresponding author.
E-mail address: mingjia@xmu.edu.cn (M. Shangguan).

https://doi.org/10.1016/j.rse.2025.114910
Received 6 September 2024; Received in revised form 25 June 2025; Accepted 9 July 2025

Churnside et al., 2017), underwater topography (Hickman and Hogg, 1969; Shangguan et al., 2023a; Steinvall et al., 1993), and underwater targets (Maccarone et al., 2023; Shangguan et al., 2024b). To expand the detection range, shipborne (Trees, 2014), airborne (Mullen et al., 1995), and even spaceborne lidars (Abdallah et al., 2012; Chen et al., 2019a) have been proposed. Additionally, to effectively avoid interference at the air-sea interface, underwater single-photon lidar has recently been introduced for ocean observation (Shangguan et al., 2024c; Shangguan et al., 2023b).

For ocean lidar system, detection depth is a crucial metric. Experimental studies indicate that the maximum detection depth of ICESat-2 can reach up to ~40 m (Parrish et al., 2019). Furthermore, dual-wavelength airborne ocean lidar has demonstrated a detection depth of around 100 m (Li et al., 2020). In contrast, shipborne photon-counting ocean lidar has shown a detection depth of 80 m (50 m) in clear (turbid) waters (Shen et al., 2022), while underwater lidar has been validated to reach up to 105 m (Shangguan et al., 2023b).

However, the depth information (termed as time-based depth profile) provided by a lidar system is based on the time that photons pass, which does not necessarily match the real depth profile. This discrepancy becomes significant when the backscattered signal contains substantial multiple-scattering contributions. For instance, studies have shown that there could be an overestimation of cloud optical thickness by up to 40 % if multiple scattering is ignored when lidar is used to detect ice clouds (Hogan, 2006). Although this phenomenon has been widely studied in the fields of cloud-profiling lidar and radar, it has received little attention in the field of ocean lidar (Mclean et al., 1998; Zege et al., 2003).

To get an in-depth understanding of this issue, this study carries out an analysis of the discrepancies between the time-based and real depth profiles caused by multiple scattering in ocean lidar. Although several methods, including the quasi-single small-angle approximation analytic methods (Kopilevich and Surkov, 2008), lidar equations considering beam spreading and pulse stretching (Mclean et al., 1998; Zege et al., 2003), and the Monte Carlo (MC) model, are widely used for simulating ocean lidar backscattered signals due to their accuracy and flexibility in handling complex scattering processes in water, this study employs the semi-analytical MC model. This model, which has been extensively applied and experimentally validated in ocean lidar signal simulations (Bissonnette et al., 2005; Chen et al., 2019b; Chen et al., 2023; D'alimonte et al., 2024; Liu et al., 2019a), is adopted here for its efficiency in recording both time-based and actual depth profiles.

Moreover, since both the time-based and the real depth profiles can be described by the attenuation coefficient and its corresponding detection depth, the discrepancy between them is quantified using the ratios of these attenuation coefficients (K_z/K_t) and depths (z^{gt}/z_d). Here, K_t and K_z are the attenuation coefficients of the time-based and real depth profiles, respectively, while z^{gt} and z_d represent the detection depths of the real and time-based depth profiles, respectively. Furthermore, for Case-1 water, assuming a vertically homogeneous water column and neglecting the influence of sea surface fluctuations, relationships are established between the ratio K_z/K_t and both scattering coefficient (b) and the radius of the receiver footprint on the water surface (r_s), as well as between the ratio z^{gt}/z_d and both b and r_s.

The structure of this article is as follows: first, the semi-analytical MC simulation, which simultaneously records time-based and real depth profiles, is introduced, with analysis focusing on six types of oceanic lidar systems from two spaceborne, two airborne, one shipborne, and one underwater platform. Subsequently, statistical model for K_z/K_t and z^{gt}/z_d in relation to the b and r_s are established for Case-1 water, assuming a vertically homogeneous column and ignoring sea surface fluctuations. The sensitivity analysis of K_z/K_t and z^{gt}/z_d to b and r_s is subsequently conducted. Moreover, the impacts of the absorption coefficient (a), scattering phase function (SPF), rough sea surface, and vertically non-uniform inherent optical properties (IOPs) on the discrepancies are further discussed. Finally, conclusions are presented.

2. Monte Carlo simulation

2.1. Semi-analytic Monte Carlo simulation

MC simulation is a statistical method used to model and analyze complex systems by generating random samples and computing results based on probabilistic principles. In lidar applications, MC simulations treat photons as particles and simulate their trajectories through water media to generate lidar backscattered signals. This approach allows for a detailed analysis of photon interactions with the water column, which is crucial for accurately modeling lidar backscattered signals. In ocean lidar applications, MC has been experimentally validated for simulating ocean signals (Liao et al., 2023; Liu et al., 2019a; Liu et al., 2019b), including elastic backscattered signals (Chen et al., 2020; Chen et al., 2018; Liu et al., 2020), inelastic backscattered signals (Spence et al., 2023), and polarization backscattered signals (Lin et al., 2023; Wu et al., 2024). To improve the computational efficiency of traditional MC simulations, this paper adopts a semi-analytic MC simulation method. In this approach, the emitted photon is treated as a large photon packet. During each scattering event, the expected value is computed and recorded to obtain the lidar backscattered profile. Here, the process of the semi-analytic MC simulation for simultaneously recording both the time-based and real depth profiles is briefly introduced. For clarity, a flowchart of the semi-analytical MC process is shown in Fig. 1, with detailed steps explained below.

First, initialize the photons with the origin of the coordinate system at the center of the laser spot incident on the water surface, where the z-axis points vertically downward and the x and y axes represent the horizontal coordinates. The initial position of the photons is set to (x_0, y_0, 0), where x_0 and y_0 are random values determined by the energy distribution of the incident laser spot on the water surface, which is considered uniform. The initial direction of the photons (u_{x0}, u_{y0}, u_{z0}) is determined based on the tilt angle of the lidar, accounting for photon refraction at the water surface, while the laser beam divergence angle is used to initialize the position of the photons on the water surface. The initial weight of the photons, W_0, is set to 1, and a threshold value, W_T, with a value of 10^{-4}, is defined for photon extinction.

During photon movement, both the step length and direction of the photons are determined by the absorption and scattering characteristics

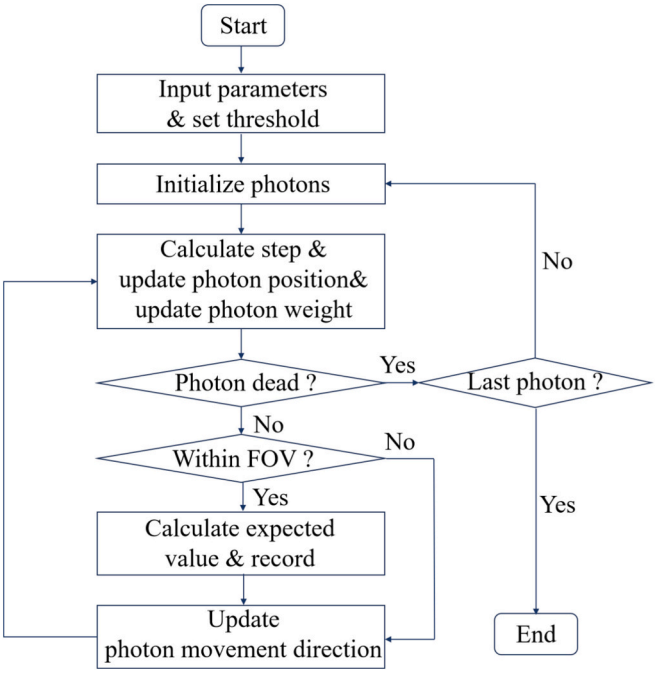

Fig. 1. Flowchart of MC simulation.

of the water. The step length (s) refers to the distance traveled by a photon during each movement, while the direction determines the specific path of the photon. The s can be expressed as:

$$s = -\ln(\xi_1)/c, \tag{1}$$

where ξ_1 is a random number uniformly distributed between 0 and 1, and c is the beam attenuation coefficient of the water. During photon movement, a portion of the energy is absorbed by the water, resulting in a decrease in weight. The updated photon weight (W_N) is given by:

$$W_N = W_{N-1} \cdot b/c, \tag{2}$$

where $W_{N\text{-}1}$ is the photon weight from the previous step.

To determine the updated location of the photon, in addition to the step length, the scattering direction of the photon also needs to be updated. The scattering direction of the photon is determined by the azimuth angle (φ) and the scattering angle (θ). The expression for φ is:

$$\varphi = 2\pi\xi_2, \tag{3}$$

where ξ_2 is a random number uniformly distributed between 0 and 1. The scattering angle, denoted as θ, is defined as the angle between the original direction of motion and the new direction after scattering. It ranges from 0 to π and is determined by the SPF $\tilde{\beta}(\theta)$. For the discrete Petzold SPF, in order to determine the scattering angle of the SPF, a lookup table is established between θ and the cumulative distribution function $F(\theta)$ based on the SPF (Chen et al., 2023). The corresponding scattering angle can be obtained through this table. The expression for $F(\theta)$ is as follows:

$$F(\theta_i) = 2\pi \sum_{j=1}^{j=i} \tilde{\beta}(\theta_j)\sin(\theta_j)\Delta\theta_j, \tag{4}$$

where j represents the index for discretely tabulated angular data and θ_j is the angle at the index j; $\Delta\theta_j$ is the angular interval between the angles from $(j-1)$ to j. In MC simulation, $F(\theta)$ is a random number ξ between 0 and 1. Find the index value that satisfies $F(\theta_{j\text{-}1}) < \xi < F(\theta_j)$, the value of scattering angle θ is obtained through linear interpolation of $\theta_{j\text{-}1}$ and θ_j.

After updating φ and θ, the updated propagation direction of the photon ($u_{x,k}$, $u_{y,k}$, $u_{z,k}$) can be obtained. If the photon's movement direction is close to the z-axis (i.e., $|u_{z,k\text{-}1}| > 0.9999$), then ($u_{x,k}$, $u_{y,k}$, $u_{z,k}$) can be updated as follows:

$$\begin{cases} u_{x,k} = \sin(\theta)\cos(\varphi) \\ u_{y,k} = \sin(\theta)\sin(\varphi) \\ u_{z,k} = SIGN(u_{z,k\text{-}1})\cdot\cos(\theta) \end{cases}, \tag{5}$$

where the $SIGN(u_{z,k\text{-}1})$ function can be expressed as:

$$SIGN(u_{z,k\text{-}1}) = \begin{cases} 1 & , u_{z,k\text{-}1} > 0 \\ -1, & u_{z,k\text{-}1} < 0 \end{cases}. \tag{6}$$

If the movement direction of the photon is not close to the z-axis (i.e., $|u_{z,k\text{-}1}| \le 0.9999$), the updated direction components ($u_{x,k}$, $u_{y,k}$, $u_{z,k}$) are expressed as:

$$\begin{cases} u_{x,k} = \sin(\theta)\cdot\dfrac{u_{x,k-1}u_{z,k-1}\cos(\varphi) - u_{y,k-1}\sin(\varphi)}{\sqrt{1-u_{z,k-1}^2}} + u_{x,k-1}\cos(\theta) \\ u_{y,k} = \sin(\theta)\cdot\dfrac{u_{y,k-1}u_{z,k-1}\cos(\varphi) + u_{x,k-1}\sin(\varphi)}{\sqrt{1-u_{z,k-1}^2}} + u_{y,k-1}\cos(\theta) \\ u_{z,k} = -\sin(\theta)\cos(\varphi)\cdot\sqrt{1-u_{z,k-1}^2} + u_{z,k-1}\cos(\theta) \end{cases}. \tag{7}$$

Given the photon's current position ($x_{k\text{-}1}$, $y_{k\text{-}1}$, $z_{k\text{-}1}$), the next step length s_k, and the movement direction of next step ($u_{x,k}$, $u_{y,k}$, $u_{z,k}$) are known, the updated position of the photon (x_k, y_k, z_k) can be expressed as:

$$\begin{cases} x_k = x_{k-1} + u_{x,k}\cdot s_k \\ y_k = y_{k-1} + u_{y,k}\cdot s_k \\ z_k = z_{k-1} + u_{z,k}\cdot s_k \end{cases}. \tag{8}$$

Subsequently, based on the updated photon weight and position, it is to determine whether the photon has been extinguished and whether it is within the receiver full-angle field of view (FOV). The updated photon weight W_N is further compared with W_T, if $W_N < W_T$, the photon is extinguished, and no further iteration is required; if $W_N \ge W_T$ and the photon is within the receiver FOV, the photon is recorded. To determine if the photon remains within the receiver FOV after scattering, it is necessary to first establish the range of the FOV.

When the laser is incident perpendicularly, with the lidar system positioned at a vertical height H above the water surface, the relationship between the FOV below the water surface (FOV′) and the FOV above the surface, after refraction at the water surface, can be expressed according to Snell's law as:

$$\mathrm{FOV}' = 2\cdot\arcsin[\sin(\mathrm{FOV}/2)/n], \tag{9}$$

where n is the refractive index of water, with a value of 1.33. For a photon at coordinates (x, y, z) to be within the FOV, it should satisfy the following conditions:

$$x^2 + y^2 \le [r_s + z\cdot\tan(\mathrm{FOV}'/2)]^2. \tag{10}$$

The tilt angle of the lidar system is denoted as α, while the laser divergence angle (typically ranging from microradians to milliradians) is much smaller in comparison. Therefore, in the simulation process, the influence of the laser divergence angle on the incident angle is neglected. The photon incident angle is treated as equivalent to the tilt angle α of the lidar system. When the lidar system is tilted, the receiver footprint on the water surface becomes elliptical. A schematic diagram is shown in Fig. 2.

As shown in Fig. 2, O represents the origin of the coordinate system on the water surface, with coordinates (0,0,0). The line segment OD is the semi-major axis of the ellipse, and its length can be expressed as follows:

$$m = \frac{H'\cdot[\tan(\alpha + \mathrm{FOV}/2) - \tan(\alpha - \mathrm{FOV}/2)]}{2}. \tag{11}$$

The distance H' from the apex of the cone, F, to the water surface, can

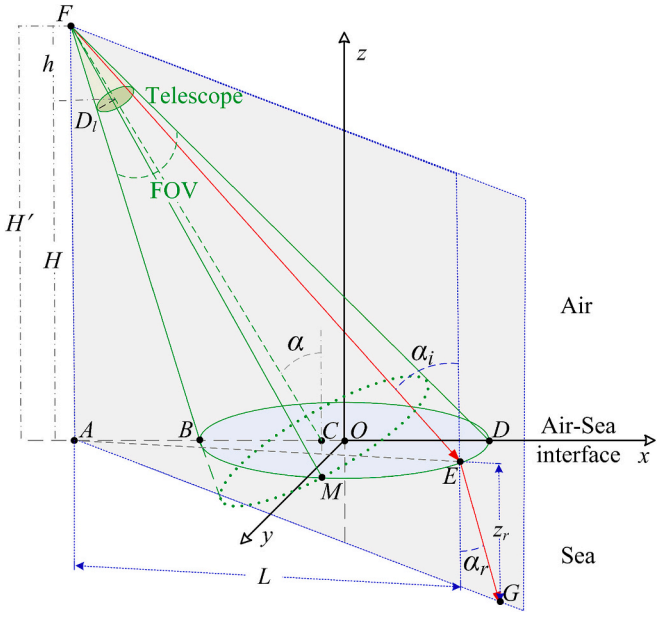

Fig. 2. Schematic diagram of a laser obliquely incident on the water surface.

be expressed as:

$$H' = H + [D_l/2{\cdot}\cos(\alpha)\,]/\tan(\mathrm{FOV}/2), \tag{12}$$

where D_l is the receiver radius of the telescope, and h, defined as (D_l/2·cosα)/tan (FOV/2), is illustrated in Fig. 2.

To determine the specific shape of the ellipse, it is necessary to identify the coordinates of any point on the ellipse besides B and D. As shown in Fig. 2, point M is a point on the water surface, located at the intersection of the circumference of the cone's base centered at point C and the water surface. Therefore, the coordinates of point M can be expressed as (x_M, y_M, 0), where the x-coordinate of point M is equal to the x-coordinate of point C, and can be expressed as:

$$x_M = l_{BC} - m = H'{\cdot}\tan\alpha - H'{\cdot}\tan(\alpha - \mathrm{FOV}/2) - m, \tag{13}$$

where l_{BC} represents the length of the line segment BC.

Since point M lies on the circular base of the cone centered at C, the length of line segment CM is the radius of the circle. Additionally, line segment MN is perpendicular to the x-axis, so the y-coordinate of point M can be expressed as:

$$y_M = H'{\cdot}\tan(\mathrm{FOV}/2)/\cos(\alpha). \tag{14}$$

Since point M lies on the ellipse of the receiver footprint on the water surface, it satisfies the following equation:

$$\frac{x_M^2}{m^2} + \frac{y_M^2}{{n_e}^2} = 1, \tag{15}$$

where n_e is the semi-minor axis length of the ellipse and can be expressed as:

$$n_e = y_M \Big/ \sqrt{1 - x_M^2/m^2}. \tag{16}$$

Assume point E is any point within the boundary of the ellipse on the receiver footprint of the water surface, with coordinates (x_E, y_E, 0). The distance L between point A (the projection of point F on the water surface) and point E, and the angle of incidence α_i at point E can be expressed as:

$$\begin{cases} L = \sqrt{(m + l_{AB} + x_E)^2 + {y_E}^2} \\ \alpha_i = \arcsin\left(L \Big/ \sqrt{(H')^2 + L^2}\right) \end{cases}, \tag{17}$$

where l_{AB} represents the length of line segment AB. According to Snell's Law, the relationship between the angle of incidence.

α_i and the angle of refraction α_r is as follows:

$$\sin\alpha_i = n{\cdot}\sin\alpha_r. \tag{18}$$

Utilizing the angle of refraction, when photons at point E propagate to point G at a depth z_r, the projection of their travel distance along the direction of line AE is dL, which can be expressed as:

$$dL = z_r{\cdot}\tan(\alpha_r). \tag{19}$$

Then, the coordinates of point G (x_G, y_G, z_r), can be expressed as:

$$\begin{cases} x_G = x_E + dL{\cdot}\cos(\omega) \\ y_G = y_E - dL{\cdot}\sin(\omega), y < 0 \\ y_G = y_E + dL{\cdot}\sin(\omega), y > 0 \\ z_r = z_r \end{cases}, \tag{20}$$

where ω is the angle between the line segment AE and the x-axis, and can be expressed as:

$$\omega = \arcsin(y_E/L). \tag{21}$$

Since point E is any point within the boundary of the ellipse on the receiver footprint of the water surface, based on this constraint and in conjunction with Eq. (20), the boundary of the underwater receiving field can similarly be derived as:

$$\begin{cases} [x - dL{\cdot}\cos\omega]^2 \Big/ m^2 + [y + dL{\cdot}\sin\omega]^2 \Big/ {n_e}^2 = 1, y < dL{\cdot}\sin(\omega) \\ [x - dL{\cdot}\cos\omega]^2 \Big/ m^2 + [y - dL{\cdot}\sin\omega]^2 \Big/ {n_e}^2 = 1, y > dL{\cdot}\sin(\omega) \end{cases}. \tag{22}$$

When photons are within the lidar's FOV, the expected photon energy E at depth z can be expressed as (Li et al., 2024; Zhou et al., 2021):

$$E(z) = \frac{A_r}{[(nH + z)/\cos(\alpha)\,]^2} \frac{\widetilde{\beta}(\theta)}{4\pi} \exp\left(- \sum_{i=1}^{i} c_i d' \right) T_a T_t W_N, \tag{23}$$

where A_r is the aperture of the telescope; H is the vertical height of lidar system; i is the i-th photon layer; c_i is the beam attenuation coefficient of the i-th layer; $d' = z/\sqrt{1 - (\sin\alpha/n)^2}$is the distance from the current scattering point to the sea surface; T_a is the atmospheric transmittance, T_t is the sea-air interface transmittance; W_N is the weight of currently scattered photon. When photons scatter, the expected value E is recorded at the corresponding position, and the weight of the photon packet is reduced accordingly. The recording method for the photon position is as follows:

$$s_p = \left(d + \sum_i s_i \right) \Big/ 2, \tag{24}$$

where s_i is the actual step length of each photon movement. The signal recorded in this manner is the time-based depth profile resulting from multiple scatterings with the water column.

However, s_p does not represent the actual depth where the lidar hits. The depth where the laser hits is z_p, which can be expressed as:

$$z_p = \sum_i z_i. \tag{25}$$

where z_i is the actual depth of each photon movement, whether it is a tilted system or a nadir viewing system. The signal recorded in this way is the real depth profile.

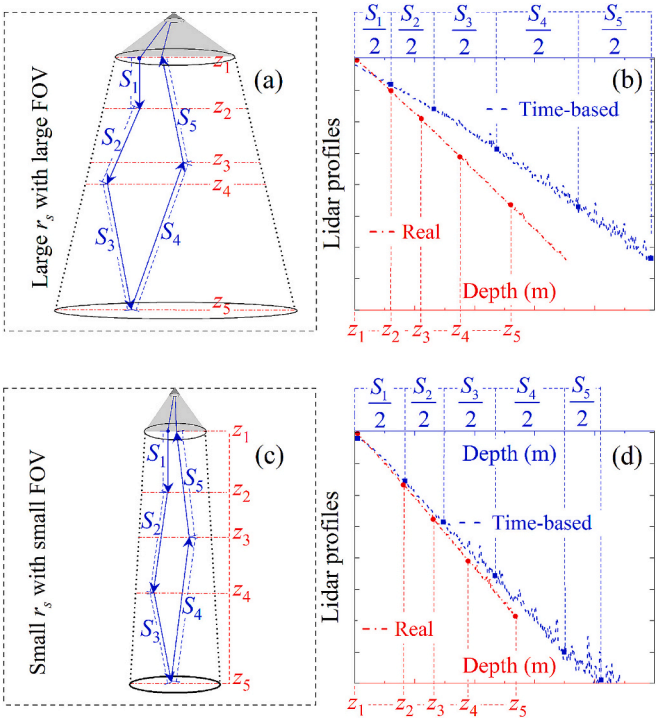

Fig. 3. Schematic diagram illustrating the differences between time-based and real depth profiles caused by multiple scattering.

To further illustrate the difference between the two profiles, Fig. 3 provides a schematic diagram, which demonstrates the impact of different r_s and FOV on the discrepancy. As shown in Fig. 3(a) and Fig. 3 (c), due to the influence of multiple scattering, there is a discrepancy between the time-based and real depth profiles. When recording the expected photon energy, if the photon position is recorded based on the movement step described in Eq. (24), the corresponding backscattered signal is the time-based depth profile. If the photon position is recorded as the true depth described in Eq. (25), the corresponding signal is the real depth profile. The profile diagrams for different FOVs are shown in Fig. 3(b) and Fig. 3(d).

As shown in Fig. 3, because of the strong forward scattering of laser beams as they travel through water, photons experience multiple scattering events during their journey. When the parameter r_s is large, as demonstrated in Fig. 3(a), the range of motion for photons within the receiver FOV increases, particularly with more photons moving laterally. As a result, the discrepancy between the travel distance of photons and their actual depth becomes more pronounced, as shown in Fig. 3(b). Consequently, for platforms with a large receiver footprint, such as spaceborne or high-altitude airborne platforms, this difference becomes significant and cannot be ignored.

For platforms with a smaller r_s and a small FOV, such as the underwater platforms and low-altitude airborne platforms, as shown in Fig. 3 (c), the scattering of photons is confined to a limited volume. Photons outside this volume cannot be received and recorded by the telescope. Consequently, although the backscattered signal contains a significant amount of multiple scattering information, the angles of these photons are primarily restricted to around 0°. Therefore, as shown in Fig. 3(d), the difference between the time-based and real depth profiles is relatively small.

2.2. Influencing factors analysis

As shown in the above analysis, discrepancies between time-based and real depth profiles are influenced by multiple factors, including the IOPs of the water—namely b, a, and SPF—as well as the illumination and reception geometry of the lidar system, such as the receiver FOV, laser incident angle, and laser divergence angle. In addition, sea surface roughness also plays a role. These factors affect the scattering angles and distributions of photons, thereby contributing to the discrepancies. For clarity, the influencing factors and their mechanisms are summarized in Table 1.

Table 1
Factors affecting discrepancy.

Parameter	Effect	Included
Laser incident angle	Larger angles increase path length and scattering, enhancing multiple scattering.	Yes
Laser divergence angle	A wider beam increases the spatial distribution of photon paths, promoting path variability and contributing to multiple scattering.	Yes
Receiver FOV	A larger FOV allows the receiver to collect more photons, including those from higher-order scattering events.	Yes
Scattering coefficient b	A higher scattering coefficient increases the number of scattering events, enhancing the multiple scattering effect.	Yes
Sea surface roughness	Surface waves modify the entry angles and spatial spread of photons, altering their underwater trajectories and increasing path variability.	Discussed
Absorption coefficient a	In highly absorbing waters, photons are rapidly attenuated, reducing the contribution from multiple scattering.	Discussed
SPF	Determines the angular distribution and intensity of scattered photons, influencing the directionality and range of scattering paths.	Discussed
Depth-dependent IOPs	Vertical variations in absorption and scattering properties affect photon propagation paths and signal shape.	Discussed

Evidently, constructing a comprehensive model that accounts for all these factors is highly challenging. Therefore, this study first simplifies the model by focusing on Case-1 water conditions, assuming vertically uniform IOPs and neglecting sea surface roughness. Under these assumptions, the relationships between the discrepancies and water IOPs and receiver FOV are analyzed while considering the effects of laser incident angle. Based on this foundation, the impacts of a, SPF, vertical variations in IOPs, and sea surface roughness on the discrepancies will be further discussed.

2.3. Bio-optical models

To simplify the simulation analysis, the bio-optical models for Case-1 waters are employed, as listed in Table 2, where λ_m represents the laser wavelength, which is set to 532 nm in this simulation. As shown in Eq. (1), the step length of photon movement is determined by c, which is the sum of a and b. The a consists of the absorption coefficient of pure water, a_w (Lee et al., 2015), the absorption coefficient of phytoplankton pigments, a_{ph} (Prieur and Sathyendranath, 1981), and the absorption coefficient of yellow substances, a_y (Lee and Tang, 2022). Additionally, b can be expressed as the sum of the scattering coefficient of pure water, b_w (Zhang and Hu, 2009) and the scattering coefficient of particles, b_p (Morel, 1988). The specific values of a and b are determined by the laser wavelength and Chl.

2.4. Key Parameters of Lidar Systems

To study the impact of multiple scattering on the detection depth, this research selected a total of six typical platforms, including spaceborne, airborne, shipborne, and underwater. The key parameters of the lidar systems for each platform are listed in Table 3.

3. Monte Carlo Results

Based on the lidar parameters from Table 3 and the water bio-optical models from Table 2 using the Petzold SPF (Petzold, 1972), with a Chl set to 0.1 mg/m^3, the simulated time-based and real depth profiles for lidar on different platforms are shown in Fig. 4. To illustrate the difference more intuitively between the real and time-based depth profiles, the MC lidar profiles in Fig. 4 and Fig. 5 have been normalized, with each profile divided by the larger of its respective maximum value.

As shown in Fig. 4, although the Chl is set to only 0.1 mg/m^3, there is a significant difference between the time-based and real depth profiles of lidar on platforms other than the underwater lidar. When the depth is shallow, the signal intensity of the real depth profile is greater than that of the time-based depth profile. However, as the depth increases, the signal intensity of the time-based depth profile surpasses that of the real depth profile, and the two profiles intersect at a certain depth. In other words, the attenuation rate of the time-based depth profile is slower than that of the real depth profile. Consequently, the maximum detection depth is overestimated when based on the time-based depth profile, meaning the actual penetration depth of ocean lidar is much shallower than the detection depth indicated by the time-based depth profile.

Additionally, as shown in Fig. 4, the differences between the time-based and real depth profiles vary across platforms, even under the same water IOPs. For the underwater platform, the time-based and real depth profiles almost completely overlap. For the airborne lidar at a flight altitude of 0.35 km, the difference between the time-based and real depth profiles is minimal. However, for platforms like CALIPSO, the differences between the time-based and real depth profiles are substantial. This indicates that the lidar parameters on different platforms influence the distribution of these discrepancies.

By decomposing the multiple scattering (MS) components in the backscattered profiles of the time-based and real depth profiles across four different platforms, the results are presented in Fig. 5. The figure

Table 2
Bio-optical models of MC simulation.

Parameter	Empirical relationships	References
Beam attenuation coefficient	$c(\lambda_m, \mathrm{Chl}) = a(\lambda_m, \mathrm{Chl}) + b(\lambda_m, \mathrm{Chl})$	–
Absorption coefficient	$\begin{cases} a(\lambda_m, \mathrm{Chl}) = a_w(\lambda_m) + 0.06A(\lambda_m)\cdot\mathrm{Chl}^{0.65} + a_y(\lambda_m, \mathrm{Chl}) \\ a_y(\lambda_m, \mathrm{Chl}) = a_y(440, \mathrm{Chl})\exp[-0.014(\lambda_m - 440)] \\ a_y(440, \mathrm{Chl}) = 0.2\left[a_w(440) + 0.06A(440)\cdot\mathrm{Chl}^{0.65}\right] \end{cases}$	Lee and Tang (2022) Lee et al. (2015) Prieur and Sathyendranath (1981)
Scattering coefficient	$\begin{cases} b(\lambda_m, \mathrm{Chl}) = b_w(\lambda_m) + b_p(\lambda_m, \mathrm{Chl}) \\ b_w(\lambda_m) = 0.0046(450/\lambda_m)^{4.32} \\ b_p(\lambda_m, \mathrm{Chl}) = 0.3\cdot\mathrm{Chl}^{0.62}(550/\lambda_m) \end{cases}$	Morel (1974) Morel (1988)
Diffuse attenuation coefficient	$\begin{cases} K_d = m_0 a + m_1[1 - m_2\exp(-m_3 a)]b_b \\ m_0 \approx 1 + 0.005\alpha \\ m_1 = 4.18, m_1 = 0.52, m_1 = 10.8 \end{cases}$	Lee et al. (2005)

Table 3
Key parameters of lidar systems.

Parameter	CALIPSO	ICESat-2	Airborne 3 km	Airborne 0.35 km	Shipborne	Underwater
Wavelength of laser	532 nm	532 nm	532 nm	532 nm	532 nm	532 nm
Photon counts	10^8	10^8	10^8	10^8	10^8	10^8
Beam spot radius of the emitted laser	2.5 mm	2.5 mm	25 mm	3.25 mm	10 mm	2 mm
Laser divergence angle	0.1 mrad	0.035 mrad	2.4 mrad	0.25 mrad	1 mrad	0.5 mrad
Laser beam spot radius on water surface	35 m	<8.7 m	3.6 m	0.4375 m	0.005 m	None
Aperture of the telescope	1000 mm	800 mm	200 mm	200 mm	50.8 mm	6 mm
FOV of the receiver	0.13 mrad	0.0884 mrad	25 mrad	6 mrad	200 mrad	3.8 mrad
Receiver footprint	92 m	45 m	75.2 m	2.3 m	2.06 m	None
Vertical height	701,000 m	500,000 m	3000 m	350 m	10 m	None
Tilt angle	8.2176°	2.0002°	3°	15°	60°	None
References	Winker et al. (2004)	Neumann et al. (2019)	Chen et al. (2021)	Chen and Pan (2019); Gordon (1982)	Zhou et al. (2022)	Shangguan et al. (2023b)

shows that, regardless of the platform, the distribution of single scattering in both the time-based and real depth profiles is identical. The difference lies in the multiple scattering signal profiles. Therefore, it can be concluded that multiple scattering is the primary cause of the discrepancy between the time-based and real depth profiles.

Additionally, for both the time-based and real depth profiles, the proportion of multiple scattering components in the total signal increases with depth. For the time-based depth profile, except for the underwater lidar, the distribution of multiple scattering initially increases and then decreases. However, for the real depth profile, the profile of multiple scattering components is monotonically decreasing. Furthermore, as depth increases, the proportion of higher-order scattering components in the time-based depth profile increases more rapidly.

Additionally, to test the MC simulations, the simulated time-based depth profiles and real-photon profiles were further analyzed as follows. For vertically homogeneous water, the lidar equation for elastic scattering can be expressed as:

$$P_m(z) = \frac{B_m Q_m(z) T_a^2 T_t^2}{[(nH + z)/\cos\alpha]^2}\cdot\beta_m\cdot\exp(-2K_{lidar}\cdot z), \tag{26}$$

where P_m represents the signal of backscattered photon at depth z received by a lidar receiver at altitude H, B_m is a constant in the elastic lidar system that does not vary with detection distance, including the pulse energy of the laser, the quantum efficiency of the detector, the telescope's receiving area, and the transmission efficiency of the optical system for both emission and reception, Q_m is the geometric overlap factor, H is the height of the lidar above the water surface, α is the tilt angle of the lidar system, β_m represents the volume scattering function at 180° at 532 nm, K_{lidar} represents the lidar attenuation coefficient at 532 nm. For a homogeneous water body, β_m can be considered constant values that do not change with depth. Although K_{lidar} exhibits slight depth dependence even within a homogeneous water column because of multiple scattering (Walker and Mclean, 1999; Zhou et al., 2019), as shown in Fig.4, to simplify the analysis, the column-averaged lidar attenuation coefficient K_{lidar} will be used in the subsequent discussions. Therefore, after obtaining the MC simulated signals, K_{lidar} can be determined using the slope method (Churnside et al., 2018).

To facilitate comparisons between different platforms, the measurement dynamic range of the lidar is limited to 60 dB, corresponding to 10^{-6}. When the time-based depth profile decays by 60 dB, the corresponding detection depth is defined as z_d, and the true depth of the photon at that point is defined as z^{gt} for vertically incident systems. The time-based and real depth profiles are truncated based on z_d and z^{gt}, respectively. Then, the lidar attenuation coefficients for the time-based depth profile (K_t) and the real depth profile (K_z) are calculated using the slope method. For the lidar system with an inclination angle of α, it is necessary to first correct the photon positions (x_i) of the time-based depth profile. The corrected photon positions (x_i') can be expressed as:

$$x_i' = x_i\cdot\cos(\alpha'), \tag{27}$$

where α' is the underwater refraction angle corresponding to the inclination angle α, which can be expressed as:

$$\alpha' = \arcsin[\sin(\alpha)/n]. \tag{28}$$

The time-based depth profile, after tilt angle correction, will be used for further calculation of z_d and K_t. Previous simulation studies show that when backscattered signals are dominated by single scattering, the

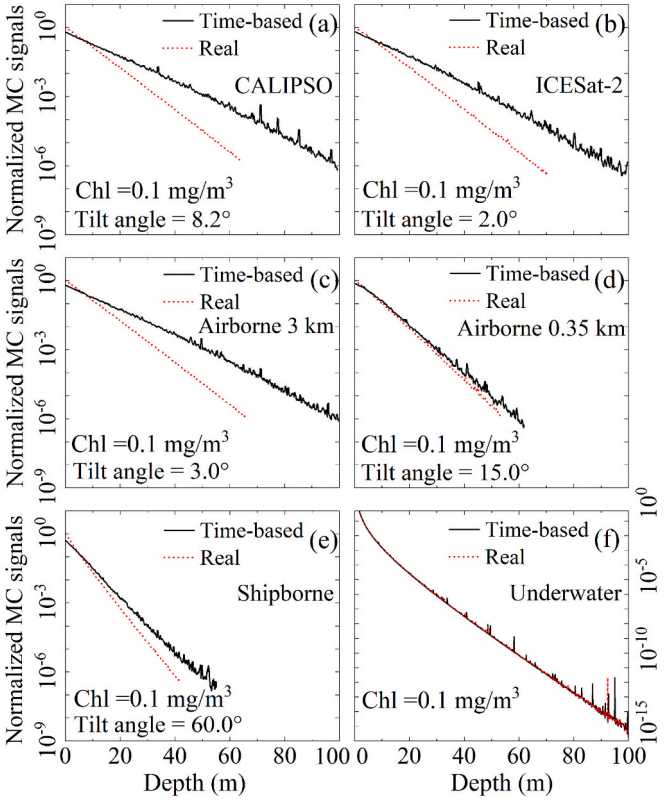

Fig. 4. Normalized MC simulated time-based depth profiles (solid lines) and real depth profiles (dashed lines) for different platforms with Chl at 0.1 mg/m^3: (a) CALIPSO, (b) ICESat-2, (c) Airborne at 3 km, (d) Airborne at 0.35 km, (e) Shipborne, and (f) Underwater.

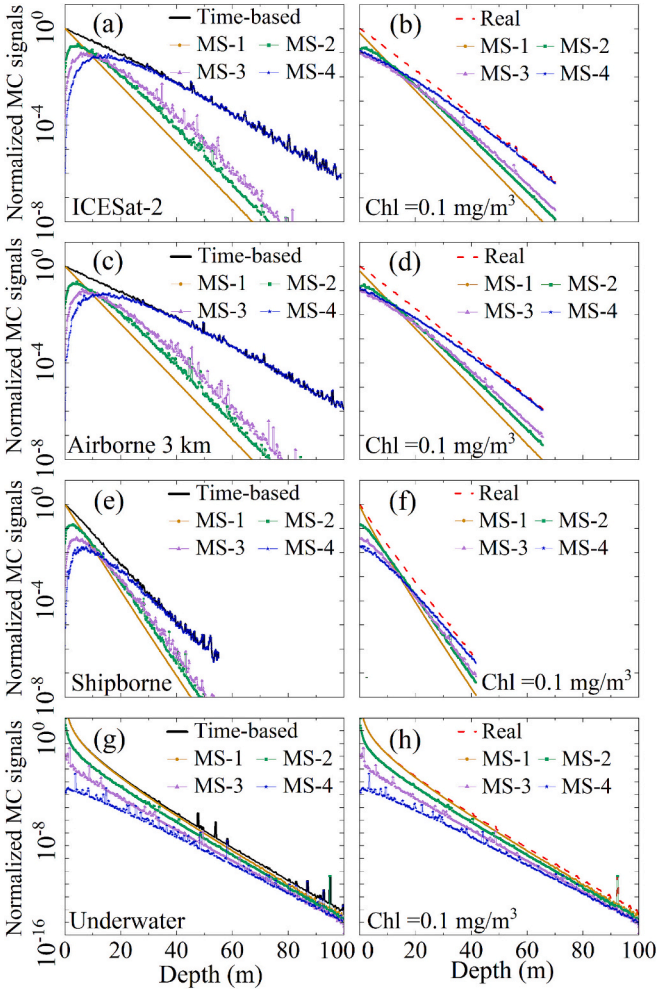

Fig. 5. Normalized MC simulated time-based depth profiles and real depth profiles for different platforms with Chl at 0.1 mg/m^3, showing profiles of multiple scattering: (a-b) ICESat-2, (c-d) Airborne at 3 km, (e-f) Shipborne, and (g-h) Underwater. In panels (a), (c), (e), and (g), solid lines represent the time-based depth profiles, while corresponding real depth profiles are shown with dashed lines in panels (b), (d), (f), and (h). MS-1, MS-2, MS-3, and MS-4 represent single scattering, double scattering, triple scattering, and four or more scattering signals, respectively.

lidar attenuation coefficient, name K_{lidar}, approaches c. In contrast, when multiple scattering dominates, K_{lidar} approximates the diffuse attenuation coefficient (K_d) (Gordon, 1982). Thus, K_t and K_z should lie between c and K_d, and this conclusion has been validated based on MC simulation (D'alimonte et al., 2024). To further test the MC simulations, K_t and K_z are compared with c and K_d for the six platforms, as shown in Fig. 6. The model of the K_d at 532 nm is determined by a and the backscattering coefficient b_b (Lee et al., 2005). The b_b can be calculated using b(532) when the SPF is defined. Note that the wavelength used in all simulations in this work is 532 nm. For simplicity, K_z, K_t, b, a, and K_d refer to the parameters at 532 nm, respectively, with the same notation used thereafter.

From Fig. 6(b), it can be observed that except for the underwater platform, the backscattered signals from the other five platforms contain a large amount of multiple scattering components, resulting in K_t being close to K_d. Although there are slight differences among the platforms due to variations in lidar hardware parameters, the relationship between K_t and K_d generally follows the 1:1 line. In contrast, for the underwater platform, K_t is significantly larger than K_d. On the other hand, from Fig. 6 (a), the K_t for the underwater platform is close to the c, while K_t for the other platforms is much smaller than c. This is consistent with the previous MC simulation results (Eidam et al., 2024; Shangguan et al., 2024d; D'alimonte et al., 2024).

Additionally, as shown in Fig. 6(c) and Fig. 6(d), the K_z values for the underwater platform are still larger than the K_z of the other five platforms. Furthermore, from the comparison between Fig. 6(b) and Fig. 6 (d), it can be observed that except for the underwater platform, where the difference between K_z and K_t is not significant, the K_z for the other five platforms is approximately twice as large as K_t. As shown in Fig. 6 (c), the K_z value for the underwater platform is closer to the 1:1 line with c, and compared to the relationship between K_t and c in Fig. 6(a), the difference between K_z and c is smaller. Moreover, the differences between K_z and c for the other five platforms are also smaller than those between K_t and c. These results suggest that the differences between K_z and K_t require further analysis.

4. Analysis of Discrepancies

4.1. K_z/K_t

To enhance simulation efficiency and emphasize the influence of multiple scattering on subsurface signals, the air-sea interface effects were neglected in the simulations. To quantitatively investigate the discrepancies between the real and time-based depth profiles, the ratios K_z/K_t and z^{gt}/z_d are introduced. According to the analysis in the previous sections, the difference is related to both water IOPs and the lidar's FOV.

To simplify the analysis, the simulation adopts the Case-1 water, where Chl can simultaneously determine a and b. Therefore, the greater the value of Chl, resulting in greater contributions of multiple scattering signals to the total lidar backscattered signal due to that there are relatively more increase in b than in a for the 532 nm wavelength. To facilitate the analysis, b is initially used to represent the contribution of

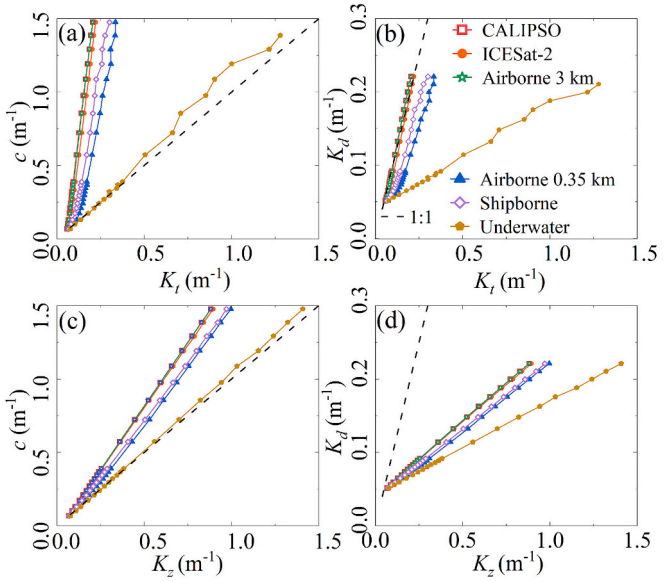

Fig. 6. Relationships of K_t and K_z, with K_d and c for six platforms: (a) c vs. K_t; (b) K_d vs. K_t; (c) c vs. K_z; (d) K_d vs. K_z.

multiple scattering caused by water IOPs, and an analysis of the impact of a on the results will be conducted subsequently. Additionally, the difference between the time-based and real depth profiles is also influenced by r_s. When the value of r_s is small, the multiple scattering angles of photons are limited to approximately 0°, and in this case, even if a significant amount of multiple scattering signal is included in the backscattered signal, it does not cause a notable difference between the time-based and real depth profiles. However, when r_s is large, the probability of lateral transmission of the laser increases, which, in turn, increases the difference between the time-based and real depth profiles. Therefore, the difference between the time-based and real depth profiles becomes significant only when both r_s and b are large.

To simplify the study, the simulation assumes a vertically homogeneous distribution of the water, allowing the slope method to calculate K_t and K_z from the MC-simulated time-based and real depth profiles. In the simulation process, the range of Chl is set from 0.01 to 10 mg/m^3 to cover a broad range of water conditions. Subsequently, the lidar parameters listed in Table 3 are input into the MC simulation, using the Petzold SPF to obtain lidar time-based and real depth profiles under different Chl values, from which K_t and K_z are calculated.

The relationship between K_z/K_t and $b{\cdot}r_s$ obtained from the MC simulation is shown in Fig. 7(a). It can be seen from the figure that the relationships between K_z/K_t and $b{\cdot}r_s$ differ across platforms. However, for the five typical platforms—CALIPSO, ICESat-2, airborne 3 km, airborne 0.35 km, and shipborne—K_z/K_t increases with increasing b, with values ranging from 1 to between 3 and 4.5. When the natural logarithms of K_z/K_t and $b{\cdot}r_s$ are taken, the results, shown in Fig. 7(b), indicate a linear relationship between the two variables. The fitting is performed using the linear function $\ln(K_z/K_t) = m_1{\cdot}\ln(b{\cdot}r_s) + n_1$, where m_1 is the slope of the fitted line, and n_1 is the intercept, with all fits having an R-squared (R^2) value exceeding 0.96.

Considering that the differences between the time-based and real depth profiles across different platforms under the same water IOPs are primarily attributed to r_s, the relationships between r_s and m_1, as well as between r_s and n_1, are established. Additionally, to provide more comprehensive data, the FOV of the lidar systems listed in Table 3 is respectively increased and decreased by a factor of two, followed by additional MC simulations. This increases the number of simulations, making the data on the relationships between r_s and m_1, and r_s and n_1 more comprehensive and generalized. The final relationships between r_s and m_1, and between r_s and n_1 are shown in Fig. 8.

As shown in Fig. 8(a), when r_s ranges from 1 m to 100 m, the variation in m_1 is small, remaining between 0.25 and 0.35. Specifically, when r_s increases from 1 to about 10 m, m_1 increases rapidly, but as r_s continues to increase, m_1 exhibits a trend of gradual change. For the relationship between n_1 and r_s, as shown in Fig. 8(b), n_1 decreases rapidly with increasing r_s, following a logarithmic trend. After fitting m_1 and r_s, as well as n_1 and r_s using logarithmic functions, the R^2 values are 0.66 and 0.98, respectively. The fitting results are as follows:

$$m_1 = 0.29 + 0.01{\cdot}\ln(r_s - 0.17). \tag{29}$$

$$n_1 = 1.00 - 0.24{\cdot}\ln(r_s + 0.07). \tag{30}$$

By substituting Eq. (29) and Eq. (30) into the linear relationship between $\ln(K_z/K_t)$ and $\ln(b{\cdot}r_s)$, an expression for K_z/K_t applicable to different lidar platforms can be derived as:

$$K_z/K_t = \exp[m_1{\cdot}\ln(b{\cdot}r_s) + n_1\,]. \tag{31}$$

Furthermore, K_z can be expressed as a function of K_t:

$$K_z = \exp[m_1{\cdot}\ln(b{\cdot}r_s) + n_1\,]{\cdot}K_t \tag{32}$$

After modifying the x-axis of Fig. 7(a) to $m_1{\cdot}\ln(b{\cdot}r_s) + n_1$–1.00, a relationship between K_z/K_t and both b and r_s applicable to different lidar platforms can be obtained, as shown in Fig. 9(a). Furthermore, the relationship between K_z/K_t and $m_1{\cdot}\ln(b{\cdot}r_s) + n_1$–1.00 can be well fitted using a quartic polynomial, with an R^2 of 0.98. It can be expressed as:

$$\frac{K_z}{K_t} = 2.83 + 3.25{\cdot}x_K + 0.69{\cdot}{x_K}^2 - 1.70{\cdot}{x_K}^3 - 0.89{\cdot}{x_K}^4 \tag{33}$$

where x_K is defined as $m_1{\cdot}\ln(b{\cdot}r_s) + n_1$–1.00.

Through the above process, the statistical model for K_z/K_t in terms of both b and r_s, specifically for Case-1 water, are established. Using Eq. (33), the distribution of K_z/K_t under varying b and r_s conditions can be plotted, as shown in Fig. 9(b). To clearly illustrate the relationship between K_z/K_t and both b and r_s, the variation of K_z/K_t with b (i.e., Chl)

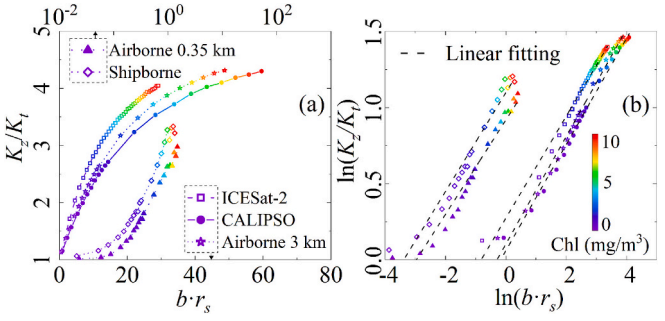

Fig. 7. Relationship between K_z/K_t and $b{\cdot}r_s$ across the range of Chl from 0.01 to 10 mg/m^3: (a) linear scale and (b) natural logarithmic scale for CALIPSO, ICESat-2, airborne 3 km, airborne 0.35 km, and shipborne platforms.

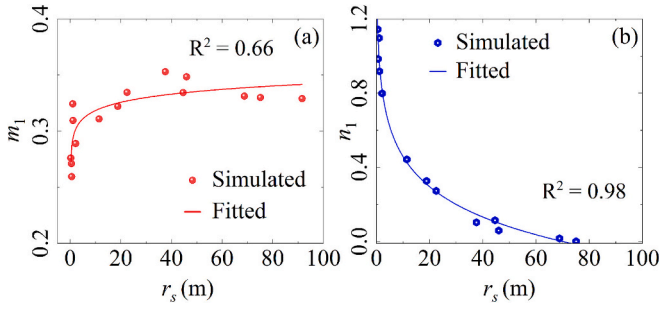

Fig. 8. Results from fitting a linear function to the curve of $\ln(K_z/K_t)$ vs. $\ln(b{\cdot}r_s)$ in Fig. 7(a) the relationship between the slope m_1 obtained from the fit and r_s, and (b) the relationship between the intercept n_1 obtained from the fit and r_s.

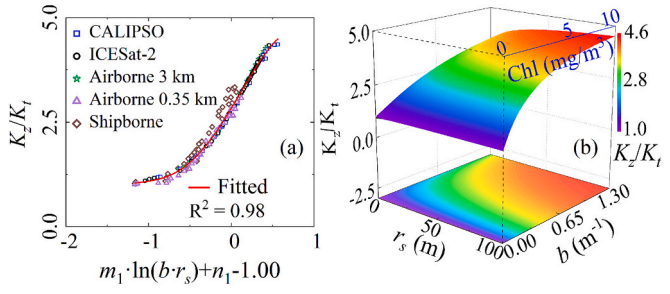

Fig. 9. (a) Distribution of K_z/K_t after modifying the x-axis of Fig. 7(a) to $m_1 \cdot \ln(b \cdot r_s) + n_1$–1.00. Symbols represent simulated results, and the red line represents the fitted curve using a polynomial function. (b) The relationship between K_z/K_t and both b and r_s, calculated using Eq. (33). (For interpretation of the references to color in this figure legend, the reader is referred to the web version of this article.)

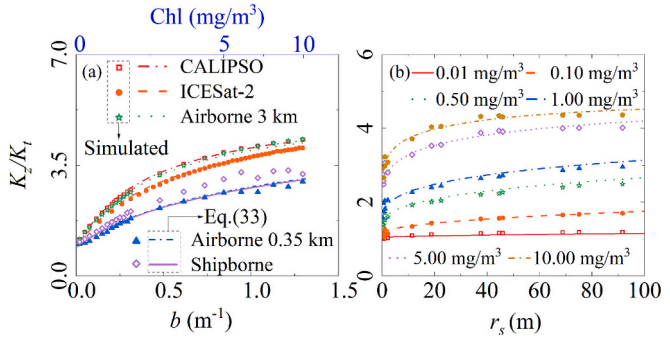

Fig. 10. (a) Variation of K_z/K_t with b (i.e., Chl) for CALIPSO, ICESat-2, airborne 3 km, airborne 0.35 km, and shipborne platforms. (b) Variation of K_z/K_t with r_s under different Chl. Symbols represent MC simulation results, and the lines represent results calculated using Eq. (33).

under different platforms in Case-1 water is shown in Fig. 10(a), while its variation with r_s under different Chl conditions is shown in Fig. 10(b). Symbols represent MC simulation results, and the lines represent results calculated using Eq. (33). It can be seen from the figures that the results from Eq. (33) are consistent with the simulation results. For shipborne platform, despite the r_s is relatively small, the larger FOV causes the receiver footprint to expand rapidly with increasing depth. This increases the probability of scattered photons moving sideways, resulting in a certain degree of error between the fitting relationship and the simulation results. Additionally, both Fig. 10(a) and Fig. 10(b) indicate that the ratio K_z/K_t increases monotonically with both b and r_s. For the shipborne platform and the airborne 0.35 km platform, where r_s is relatively small, the range of K_z/K_t is between 1 and 3.5. In contrast, for the airborne 3 km, ICESat-2, and CALIPSO platforms, where r_s is larger, the range of K_z/K_t is broader, spanning from 1 to 4.5. Moreover, a comparison of Fig. 10(a) and Fig. 10(b) shows that K_z/K_t is more sensitive to changes in b than to changes in r_s. Furthermore, when Chl is low, such as 0.01 mg/m^3 and 0.1 mg/m^3, the effect of r_s on K_z/K_t is minimal. Fig. 10(b) shows that the minimum value of K_z/K_t is determined by b. As Chl increases, K_z/K_t becomes more sensitive to changes in r_s, particularly when $r_s \leq 50$ m, where K_z/K_t increases monotonically with r_s. As r_s continues to increase, the changes in K_z/K_t begin to saturate and stabilize.

4.2. z^{gt}/z_d

The detection depth of lidar is an important metric. From the above analysis, the attenuation coefficient K_t of the time-based depth profile is smaller than the attenuation coefficient K_z of the real depth profile. It indicates that the attenuation rate of the time-based depth profile is slower than that of the real depth profile, causing the calculated detection depth (z_d) from the time-based profile to be greater than the real detection depth (z^{gt}), thus leading to an overestimation of the detection depth. Since the attenuation rate of the lidar signal determines the detectable depth, z^{gt}/z_d can be calculated from K_z/K_t. As shown in Fig. 11(a), there is a negative correlation between z^{gt}/z_d and K_z/K_t. Based on this relationship, z^{gt}/z_d can be obtained from K_z/K_t using the following equation:

$$z^{gt} \Big/ z_d = (K_z/K_t)^{-1} \tag{34}$$

Through the above process, the expressions for z^{gt}/z_d are established, for Case-1 waters. Using Eq. (34), the distribution of z^{gt}/z_d under varying b and r_s conditions can be plotted, as shown in Fig. 11(b). To clearly illustrate the relationship between z^{gt}/z_d and both b and r_s, the variation of z^{gt}/z_d with b under different platforms is shown in Fig. 12(a), while its variation with r_s under different Chl conditions is shown in Fig. 12(b). Symbols represent MC simulation results, and the lines represent results calculated using Eq. (34). It can be seen from the figures that the results from Eq. (34) are consistent with the simulation results.

As shown in Fig. 12, similar to the relationship between K_z/K_t and both b and r_s in Fig. 10, z^{gt}/z_d is more sensitive to changes in b than to those in r_s. When b is less than 0.3 m^{-1}, z^{gt}/z_d is particularly sensitive to b. For example, when b increases from 0 to 0.3 m^{-1}, z^{gt}/z_d decreases from nearly 1 to 0.5, indicating that the actual detection depth is only 50 % of the time-based depth. As b increases, the changes in z^{gt}/z_d become more stable. In contrast, as shown in Fig. 12(b), the effect of r_s on z^{gt}/z_d is relatively small; z^{gt}/z_d decreases slowly as r_s increases from about 1 m to 100 m. The minor fluctuations in z^{gt}/z_d with r_s may be attributed to a lower signal-to-noise ratio (SNR) in the MC simulation.

For the underwater lidar with parameters listed in Table 3, due to the small FOV and the system is submerged underwater, the difference between the time-based and real depth profiles is minimal. As Chl varies from 0.01 to 10 mg/m^3, the relationships between K_z/K_t and b, and between z^{gt}/z_d and b for the underwater lidar are shown in Fig. 13(a) and Fig. 13(b), respectively. As shown in Fig. 13, when the Chl is low, e.g., less than 5 mg/m^3, the K_z/K_t and z^{gt}/z_d values for the underwater lidar approach 1. This indicates that the difference between the time-based and real depth profiles is minimal. However, as the Chl increases, the differences between K_t and K_z, as well as between z^{gt} and z_d, become more pronounced. When the Chl reaches 10 mg/m^3, K_z/K_t is about 1.35, and z^{gt}/z_d is about 0.62. Therefore, in most oceanic regions where Chl < 5 mg/m^3, the measurements from the underwater lidar closely represent the distribution of photons at different depths. However, when Chl exceeds 5 mg/m^3, the underwater lidar measurements deviate significantly from the real depth profile and require correction.

4.3. Analysis of the statistical models

To validate the accuracy of Eq. (33) and Eq. (34), MC simulations

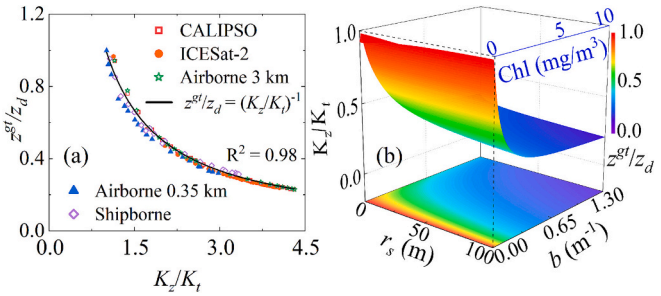

Fig. 11. (a) The relationship between z^{gt}/z_d and K_z/K_t. Symbols represent simulated results, and the black line represents the reciprocal of K_z/K_t. (b) The relationship between K_z/K_t and both b and r_s, calculated using Eq. (34).

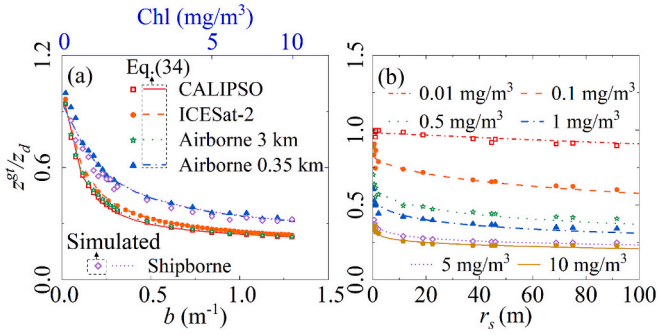

Fig. 12. Similar to Fig. 10, but (a) shows z^{gt}/z_d vs. b and (b) shows z^{gt}/z_d vs. r_s instead of K_z/K_t with b and r_s.

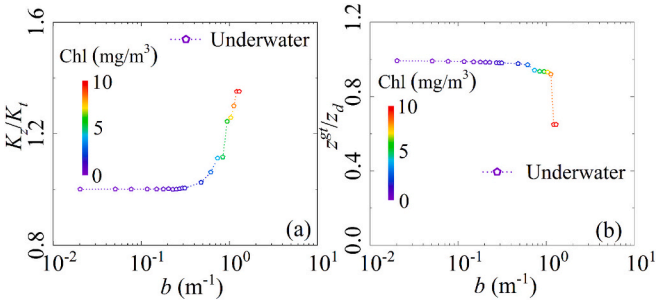

Fig. 13. (a) K_z/K_t vs. $b{\cdot}r_s$ and (b) z^{gt}/z_d vs. $b{\cdot}r_s$ as Chl ranges from 0.01 to 10 mg/m^3, for the underwater platform.

were conducted using Chl not included in the model construction. The K_z/K_t and z^{gt}/z_d results from the re-run MC simulations were compared with the corresponding model-predicted values to quantify the model's prediction errors. Specifically, K_z/K_t and z^{gt}/z_d derived from the MC simulation are denoted as K_s and z_s, respectively, while the corresponding model-predicted values are denoted as K_p and z_p. The prediction errors for K_z/K_t and z^{gt}/z_d, denoted as $Error_K$ and $Error_z$, respectively, are calculated using the following equations:

$$Error_K = |K_s - K_p|/K_p \times 100\% \quad (35)$$

$$Error_z = |z_s - z_p|/z_p \times 100\% \quad (36)$$

As shown in Fig. 14, the model exhibits strong predictive accuracy across different platforms, with the prediction errors ($Error_K$ and $Error_z$) remaining below 15 % even across a wide range of Chl variations.

To assess the model's sensitivity, partial derivatives of Eq. (33) and Eq. (34) with respect to b and r_s were carried out, and the results are shown in Fig. 15 and Fig. 16. As illustrated in Fig. 15(a)and Fig. 16(a), as b increases, $\partial(K_z/K_t)/\partial(b)$ and $\partial(z^{gt}/z_d)/\partial(b)$ decrease. This indicates that K_z/K_t and z^{gt}/z_d are more sensitive to changes in b when b is small, but as

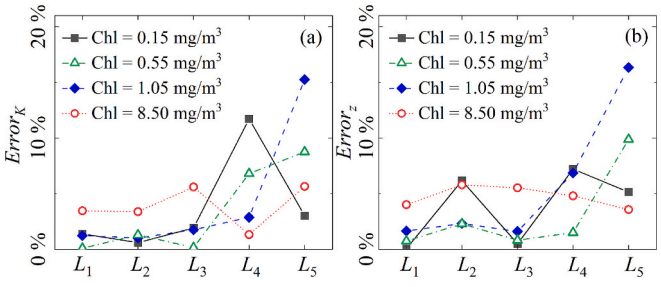

Fig. 14. $Error_K$(a) and $Error_K$(a) for different Chl and platform, where $L_1 \sim L_5$ represent CALIPSO、ICESat-2、Airborne 3 km、Airborne 0.35 km、Shipborne respectively.

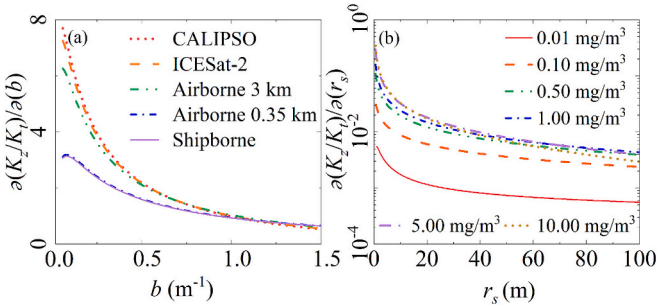

Fig. 15. (a) Partial derivative of K_z/K_t with respect to b using Eq. (33) for CALIPSO, ICESat-2, airborne 3 km, airborne 0.35 km, and shipborne platforms. (b) Partial derivative of K_z/K_t with respect to r_s under different Chl using Eq. (33).

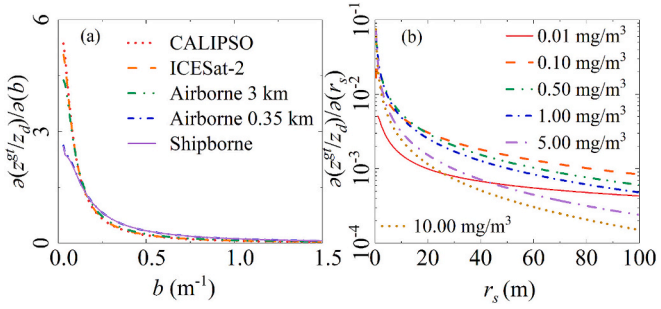

Fig. 16. Similar to Fig. 15, but (a) shows $\partial(z^{gt}/z_d)/\partial(b)$ vs. b and (b) shows $\partial(z^{gt}/z_d)/\partial(r_s)$ vs. r_s.

b increases, the sensitivity weakens, leading to the stabilization of K_z/K_t and z^{gt}/z_d. A similar pattern is observed for r_s, as shown in Fig. 15(b) and Fig. 16(b). Comparing Fig. 15(a) with Fig. 15(b) and Fig. 16(a) with Fig. 16(b), it can be concluded that K_z/K_t and z^{gt}/z_d are much more sensitive to changes in b than to changes in r_s, meaning that K_z/K_t and z^{gt}/z_d are more strongly influenced by b.

5. V. Discussion of the Influence of Other Parameters

5.1. Effect of Absorption Coefficient

For Case-1 waters, the IOPs can be calculated using Chl, which allows b to effectively represent the IOPs of the water, thereby establishing statistical models for K_z/K_t and z^{gt}/z_d. However, as the a is a key component of c, it is evident from Eq. (1) that the absorption coefficient a influences the average photon path length ($\bar{s}$) and also affects the single scattering albedo (b/c), which in turn impacts photon attenuation and the distribution of multiple scattering. Therefore, it is necessary to analyze the effect of changes in a on K_z/K_t and z^{gt}/z_d. To investigate the model's applicability in non-Case-1 waters and evaluate the impact of the absorption coefficient a on K_z/K_t and z^{gt}/z_d, two sets of MC simulation experiments were conducted under three Chl: 0.01 mg/m^3, 0.1 mg/m^3, and 1 mg/m^3. In the first set, the scattering coefficient b was held constant while varying a from 0 to 2 times the Case-1 water model value. In the second set, a was fixed while b was varied within the same range. The corresponding simulation results are presented in Fig. 17 and Fig. 18. Two representative lidar platforms are selected for the analysis. The first is the spaceborne ICESat-2, which features a small incident angle and a large r_s. The second is a 0.35 km airborne platform, characterized by a large incident angle and a small r_s. These two platforms are also employed in the subsequent analyses to discuss the effects of different SPFs, sea surface roughness, and depth-dependent IOP variations on the discrepancies.

As shown in Fig. 17 and Fig. 18, for both spaceborne and airborne

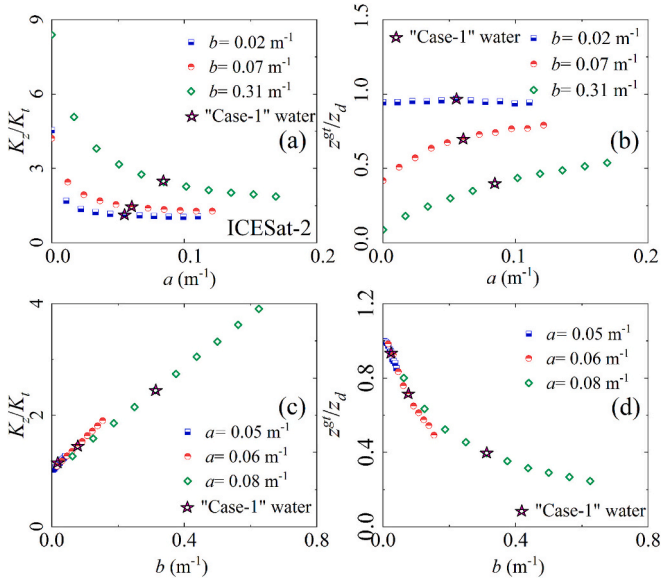

Fig. 17. Effect of a on K_z/K_t (a) and z^{gt}/z_d (b), and effect of b on K_z/K_t (c) and z^{gt}/z_d (d) under three b and a value, respectively, for the ICESat-2 platform.

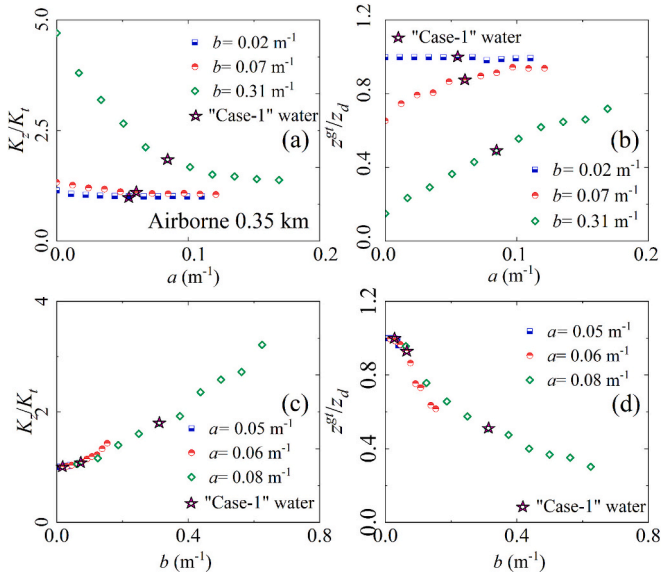

Fig. 18. Similar to Fig. 17, but for the airborne 0.35 km platform.

lidar platforms, and regardless of the value of b, an increase in a, with b held constant, causes K_z/K_t and z^{gt}/z_d to converge towards 1. This is because the increase in a leads to a rise in c, thereby reducing the photon step length (s), and also lowers the b/c ratio, which accelerates photon weight attenuation. Both factors limit the penetration depth of photons, suppressing the multiple scattering effect, which reduces the difference between the time-based depth signal and the real depth signal, ultimately causing K_z/K_t and z^{gt}/z_d to converge towards 1.

However, when a remains constant, increasing b causes K_z/K_t and z^{gt}/z_d to gradually deviate from 1. This is because a higher b increases the ratio b/c, leading to slower photon attenuation and more scattering events. As a result, multiple scattering effects are intensified, thereby enlarging the discrepancy between the time-based depth signal and the actual depth.

Finally, for Case-1 waters, where both a and b are determined by Chl, K_z can be evaluated using Eq. (33), and z^{gt} can be assessed based on Eq. (34). For other waters, the effect of the absorption coefficient a should be considered.

5.2. Effect of scattering phase function

The SPF determines the distribution of the light field underwater (Churnside and Shaw, 2020), which in turn affect the distribution of K_z/K_t and z^{gt}/z_d. To investigate the influence of different SPFs on K_z/K_t and z^{gt}/z_d, this work incorporates the Henyey-Greenstein (HG) SPF, which significantly differs from the previously used Petzold SPF, for conducting the MC study. The HG function can be expressed as (Henyey and Greenstein, 1941):

$$\widetilde{\beta}_p = \frac{1}{4\pi}\frac{1-g^2}{[1+g^2-2g\cos(\theta)]^{3/2}} \tag{37}$$

where g is the asymmetry factor, ranging from −1 to 1. When $g = 0.919$, this function yields the same backscattering ratio (B_P) as the Petzold SPF (Churnside and Shaw, 2020). B_P is a key parameter in ocean optics, closely related to the optical properties of water, and represents the probability of photon backscattering ($\theta \geq 90°$). It is calculated as follows (Liu et al., 2020):

$$B_P = b_{bp}/b_p, \tag{38}$$

where b_{bp} is the particulate backscattering coefficient, and b_p is the total particulate scattering coefficient. For the HG SPF, B_P depends on the value of the asymmetry factor g (Mobley et al., 2002):

$$B_P = \frac{1-g}{2g}\left(\frac{1+g}{\sqrt{1+g^2}}-1\right). \tag{39}$$

In typical ocean waters, the B_P generally ranges from 0.005 to 0.03 (Mobley et al., 2002). To examine the impact of different SPFs on the simulation results, the ICESat-2 platform was used as an example. Three g values were selected: 0.919, 0.880, and 0.975, corresponding to B_P values of 0.0183, 0.0280, and 0.0053, respectively. These SPFs are referred to as HG_1, HG_2, and HG_3.

Fig. 19(a) compares the Petzold SPF with the HG SPFs under different g values. For forward scattering angles less than 5°, HG_1 and HG_2 show significantly lower values than the Petzold SPF, while differences in the backward direction are relatively small. HG_3 exhibits more substantial deviations from the Petzold SPF: at angles below 1° and from 8° to 180°, the Petzold SPF is noticeably stronger. Furthermore, the Petzold SPF increases monotonically from 135° to 180°, whereas HG_3 decreases monotonically.

The cumulative distribution functions $F(\theta)$ for each SPF are shown in Fig. 19(b). According to Eq. (4), in each scattering event, a random value between 0 and 1 is drawn for $F(\theta)$, which determines the photon's scattering angle. As shown in the figure, for the same $F(\theta)$, HG_2 yields the largest θ, followed by HG_1. When $\theta < 1°$, HG_3 produces larger angles than the Petzold SPF, while for $\theta > 1°$, HG_3 yields the smallest angles.

To demonstrate the influence of different SPFs on the lidar backscattered signal, photon scattering trajectories for the ICESat-2 platform were compared for Chl of 0.10 mg/m^3 and 1.00 mg/m^3, as shown in Fig. 19(c) and (d). Note that the single photon trajectory is inherently random and is presented here solely to clearly illustrate the underlying principles. During the simulation, all SPFs shared the same photon step length and $F(\theta)$ for each scattering event, with only the scattering angle varying to reflect the angular characteristics of different SPFs. As shown in Fig. 19(c) and (d), since HG_3 generally produces smaller scattering angles, the corresponding photon paths are longer.

The resulting MC signals for the two Chl conditions of ICESat-2 and Airborne 0.35 km platforms are shown in Fig. 19(e-h). For all cases, HG_3 yields the largest z^{gt} and z_d, indicating the longest signal propagation and greatest penetration depth. However, the differences in z^{gt}/z_d among different SPFs are minimal, with deviations from the Petzold SPF remaining below 10 %, as shown in Table 4. Although different SPFs

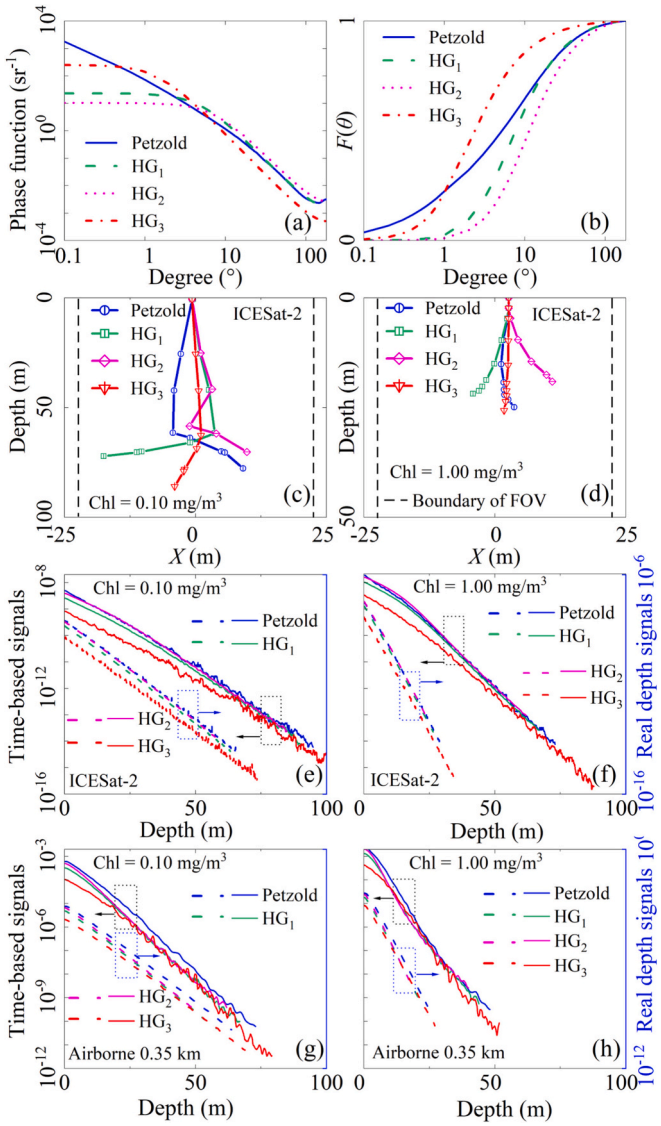

Fig. 19. Comparison four different SPFs (a) and their corresponding $F(\theta)$ functions (b), where solid line represents Petzold, while dashed lines represent HG with different g. (c)-(d): schematic photon trajectories under different SPFs for ICESat-2 at Chl = 0.10 mg/m^3 and 1.00 mg/m^3, respectively. (e)-(f): MC results under different SPFs for ICESat-2 at Chl = 0.10 mg/m^3 and 1.00 mg/m^3, where solid lines indicate time-based signals and dashed lines indicate real depth signals. (g)-(h): As in (e)-(f), but for Airborne 0.35 km platform.

cause variations in lidar penetration depth, when using the HG SPF with B_P values ranging from 0.005 to 0.03, the impact on the ratio z^{gt}/z_d is relatively small.

To specifically compare the differences in the statistical models under different SPFs, the HG$_1$ model was used, and the relationship between K_z/K_t and both b and r_s is recalculated as follows:

$$K_z/K_t = \exp[m_2 \cdot \ln(b \cdot r_s) + n_2], \tag{40}$$

where m_2 and n_2 are functions of r_s, and can be expressed as follows:

$$m_2 = 0.32 + 2.16 \times 10^{-3} \cdot \ln(r_s - 0.28). \tag{41}$$

$$n_2 = 0.96 - 0.22 \cdot \ln(r_s - 0.13). \tag{42}$$

Similarly, the relationship between z^{gt}/z_d and K_z/K_t under the HG$_1$ can also be represented by Eq. (34).

To quantitatively analyze the MC results obtained with the Petzold and HG$_1$ SPFs, the relative errors between K_z/K_t and z^{gt}/z_d obtained using the Petzold SPF and those obtained using the HG$_1$ SPF are defined as $\Delta(K_z/K_t)$ and $\Delta(z^{gt}/z_d)$, respectively. The equations are as follows:

$$\Delta(K_z/K_t) = \left| \frac{(K_z/K_t)_p - (K_z/K_t)_{hg}}{(K_z/K_t)_p} \right| \times 100\%, \tag{43}$$

$$\Delta(z^{gt}/z_d) = \left| \frac{(z^{gt}/z_d)_p - (z^{gt}/z_d)_{hg}}{(z^{gt}/z_d)_p} \right| \times 100\%, \tag{44}$$

where the subscripts p and hg represent the simulation results obtained using Petzold SPF and HG$_1$ SPF, respectively.

Their distributions of $\Delta(K_z/K_t)$ and $\Delta(z^{gt}/z_d)$ with respect to both b and r_s are shown in Fig. 20. The results in Fig. 20 indicate that the differences between the results from the two SPFs are minimal. For Chl ranging from 0 to 10 mg/m^3 and r_s ranging from 0 to 100 m, $\Delta(K_z/K_t)$ and $\Delta(z^{gt}/z_d)$ remain within 10 %. Overall, whether the water is represented by the Petzold or HG$_1$, despite some differences between them, the conclusion remains consistent: when the r_s and water's b are large, the differences between the time-based profile and the real depth profile are significant.

Table 4
Simulation results of different SPF.

Platform	Chl (mg/m^3)	SPF	z^{gt}/z_d	Relative deviation vs. Eq. (34)
ICESat-2	0.1	Petzold	0.702	1.30 %
		HG$_1$	0.704	1.59 %
		HG$_2$	0.695	0.29 %
		HG$_3$	0.716	3.32 %
	1.0	Petzold	0.398	0.25 %
		HG$_1$	0.395	0.50 %
		HG$_2$	0.392	1.26 %
		HG$_3$	0.396	0.25 %
Airborne 0.35 km	0.1	Petzold	0.874	5.62 %
		HG$_1$	0.868	4.91 %
		HG$_2$	0.825	0.28 %
		HG$_3$	0.870	5.16 %
	1.0	Petzold	0.507	6.66 %
		HG$_1$	0.490	9.92 %
		HG$_2$	0.475	12.61 %
		HG$_3$	0.526	3.20 %

5.3. Effect of sea surface roughness

Surface waves alter the laser incident angle and the transmittance and reflectance at the air–sea interface, thereby affecting the underwater photon paths, the incident energy, and the strength of the surface backscatter. To analyze the impact of a rough sea surface on subsurface profile signals, a rough surface model is established in this section, focusing on the effects of transmittance variation and incident angle changes, while excluding the simulation of surface backscatter. First, the Pierson–Moskowitz (PM) spectrum is used to describe the energy distribution of ocean waves. The PM spectrum is a complex sinusoidal wave model, and the variation of energy spectral density with angular frequency can be expressed as (Pierson Jr and Moskowitz, 1964):

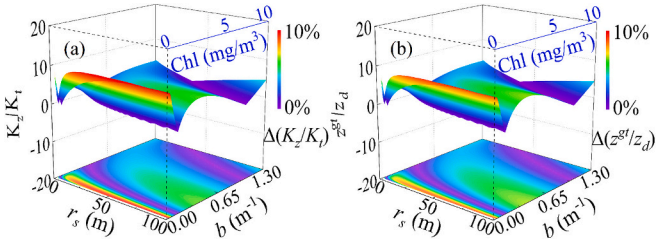

Fig. 20. (a) $\Delta(K_z/K_t)$ and (b) $\Delta(z^{gt}/z_d)$ distribution with respect to both b and r_s.

$$P(w) = \frac{A \cdot g_0^2}{w^5} \exp\left[-B\left(\frac{g_0}{U \cdot w}\right)^4 \right], \tag{45}$$

where w denotes the angular frequency of ocean waves; A and B are constants of the Pierson–Moskowitz (P-M) spectrum, with values of 8.1 $\times 10^{-3}$ and 0.74, respectively. g_0 is the gravitational acceleration, taken as 9.81 m/s^2. U represents the wind speed at 19.5 m above the sea surface (unit: m/s) and is the only variable parameter in the P-M spectrum.

Additionally, the directional spreading function $\psi(\theta)$ is expressed as:

$$\psi(\theta) = \frac{2}{\pi}\cos^2(\theta), \; -\frac{\pi}{2} < \theta < \frac{\pi}{2} \tag{46}$$

where θ is the angle between the wave propagation direction and the wind direction. The distribution of θ is independent of the angular frequency w. The wave spectrum function includes both wave direction and wave frequency, represented as the product of these two independent functions (Chen et al., 2022):

$$\begin{aligned} S(w,\theta) &= P(w)\cdot\psi(\theta) \\ &= \frac{A \cdot g_0^2}{w^5} \exp\left[-B\left(\frac{g_0}{U \cdot w}\right)^4 \right] \times \frac{2}{\pi}\cos^2(\theta). \end{aligned} \tag{47}$$

To fully characterize the sea surface elevation in three-dimensional space, each wave component must incorporate spatial propagation terms. For a given frequency w_n and direction θ_n, the wavenumber k_n is determined by the dispersion relation as follows:

$$k_n = w_n^2 / g_0. \tag{48}$$

The projections of the x-coordinate and y-coordinate are given as follows, respectively:

$$\begin{cases} k_{x,n} = k_n \cos\theta_n \\ k_{y,n} = k_n \sin\theta_n \end{cases} \tag{49}$$

The ocean surface can be considered as the linear superposition of multiple wave components with different frequencies, directions, amplitudes, and phases. The resulting linear wave function represents the surface elevation at each point. In practical applications, the wave spectrum is expressed as (Chen et al., 2022):

$$\zeta(x,y,t) = \sum_{n=1}^{\infty} \sqrt{2S(w_n,\theta_n)\delta_w} \cdot \cos\left(k_{x,n}x + k_{y,n}y - w_n t + \varepsilon_n\right), \tag{50}$$

where x and y are the two-dimensional plane coordinates along the wind speed direction and perpendicular to the wind speed direction, respectively, $\delta_w = w_n - w_{n-1}$ denotes the frequency interval, w_n is the wave angular frequency, and ε_n is a random phase.

To investigate the influence of sea surface roughness on K_z/K_t and z^{gt}/z_d, the ICESat-2 platform is taken as an example. The wave frequency w_n is set from 0.01 to 3 rad/s to cover wave characteristics from long to short wavelengths, with a frequency interval δ_w of 0.02 rad/s. Wind speeds U are set to 0 m/s, 10 m/s, and 20 m/s, and sea surface waveforms at $t = 0$ are randomly generated, and the wave cross-section along the x-axis direction is shown in Fig. 21(a) and (b). When photons penetrate the sea surface at random positions, their propagation directions change due to refraction at the rough interface.

During the simulation, the initial horizontal positions of photons (x_0, y_0) and the movement step length in each scattering event are set to be the same under different wind speeds U, while the initial vertical position z_0 and the initial refraction angle vary according to the corresponding sea surface slope. Taking Chl of 0.10 mg/m^3 and 1.00 mg/m^3 as examples, representative photon scattering trajectories for ICESat-2 are shown in Fig. 21(c) and (d). Under calm sea conditions ($U = 0$ m/s), photons exhibit the longest propagation paths, while under $U = 20$ m/s, the penetration depth is the shallowest. The MC signals from both ICESat-2 and the Airborne 0.35 km platform, as shown in Fig. 21(e–f) and (g–h), respectively, also confirm that lidar penetration becomes shallower with increasing wind speed U, due to the enhanced sea surface roughness. Nevertheless, the variations in z^{gt}/z_d under different wind speeds U are minor, with deviations from the statistical model (Eq. (34)) remaining below 10 %, as shown in Table 5. Therefore, it can be inferred

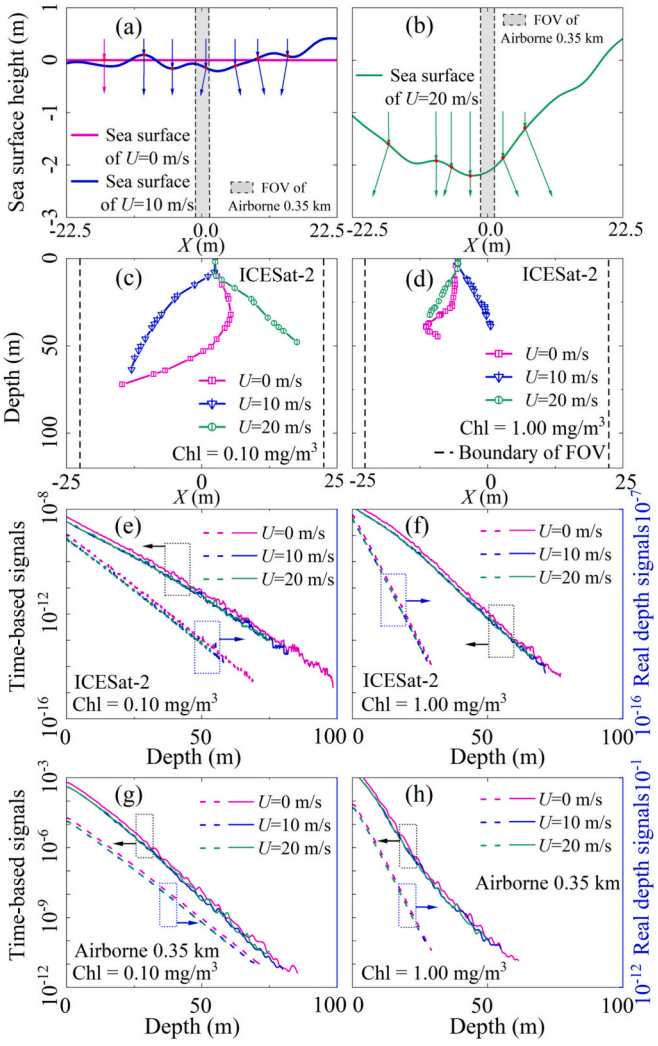

Fig. 21. Sea surface roughness patterns under different wind speeds: (a) $U = 0$ m/s and 10 m/s, (b) $U = 20$ m/s; arrows indicate refracted photon paths at different incident positions. (c), (d) Photon trajectory diagrams at Chl = 0.10 mg/m^3 and 1.00 mg/m^3 of ICESat-2, respectively. (e), (f) Corresponding MC signals of ICESat-2, where solid lines represent time-based signals and dashed lines represent real-depth signals. Note that surface backscatter is not included in this simulation. (g)-(h): As in (e)-(f), but for Airborne 0.35 km platform.

Table 5
Simulation results of different wind speed.

Platform	Chl (mg/m^3)	U (m/s)	z^{gt}/z_d	Relative deviation vs. Eq. (34)
ICESat-2	0.1	0	0.705	1.73 %
		10	0.710	2.45 %
		20	0.709	2.31 %
	1.0	0	0.392	1.26 %
		10	0.398	0.25 %
		20	0.395	0.50 %
Airborne 0.35 km	0.1	0	0.849	2.62 %
		10	0.869	4.99 %
		20	0.803	2.94 %
	1.0	0	0.477	9.96 %
		10	0.500	5.66 %
		20	0.486	8.38 %

that although sea surface roughness affects the absolute detection depth, its impact on the ratio z^{gt}/z_d is limited.

5.4. Effects of depth-dependent IOP variations

When the IOPs of the water column are vertically non-uniform, light propagation in the stratified water body becomes more complex. The presence of stratification alters the propagation path of light and enhances multiple scattering effects, thereby increasing the discrepancy between time-based signals and real depth signals.

To investigate the impact of vertically non-uniform IOPs on the ratios K_z/K_t and z^{gt}/z_d, lidar backscattered signals under different Chl distributions were simulated using the ICESat-2 and Airborne 0.35 km platforms as examples, as shown in Fig. 22. In the simulations, the background Chl was set to 0.1 mg/m^3, with a peak value of 0.5 mg/m^3.

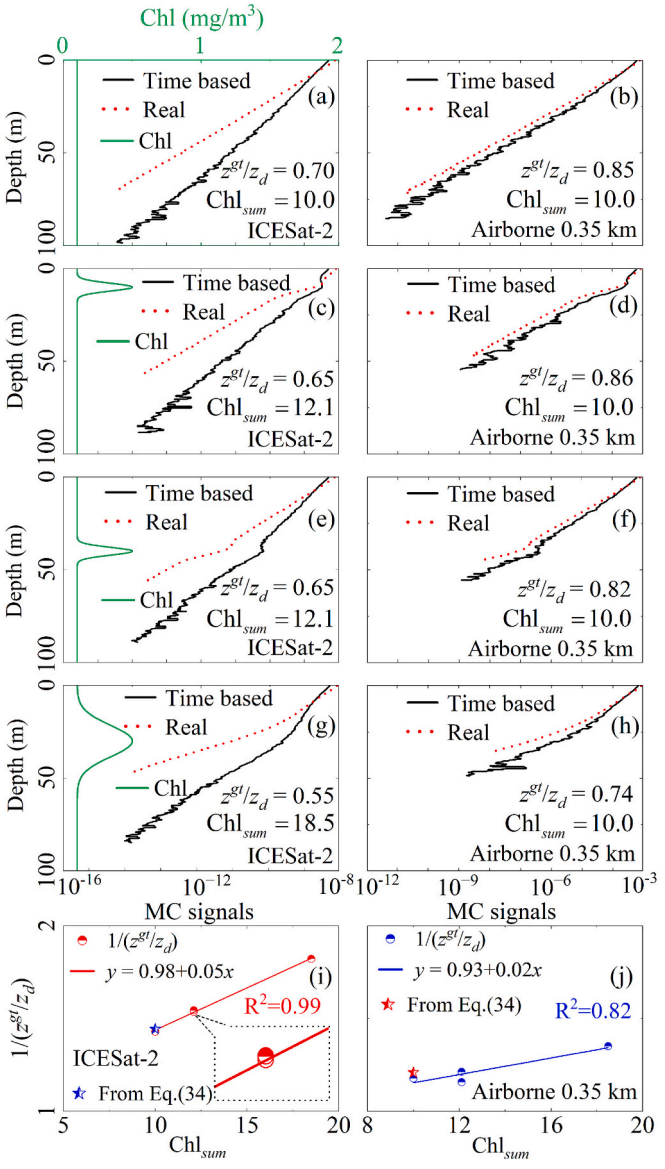

Fig. 22. Analysis of the effect of vertical IOPs distribution on statistical models. Vertical Chl distributions: (a) uniform, (c) shallow thin scattering layer, (e) deep thin scattering layer, and (g) thick scattering layer. Corresponding MC signals for ICESat-2 are shown in (a), (c), (e), and (g), while MC signals of the Airborne 0.35 km platform are shown in (b), (d), (f), and (h), where solid lines represent time-based signals and dotted lines represent real depth signals. Relationships between the vertical integral of Chl and 1/(z^{gt}/z_d) for (i) ICESat-2 and (j) the Airborne 0.35 km platform.

The position and thickness of the peak layer were varied accordingly.

To facilitate comparison, the MC results for uniform Chl distribution (Fig. 22(a)) are shown in Fig. 22(a)-(b). For cases involving a thin, high-concentration Chl layer with a full width at half maximum (FWHM) of 5 m, the peak positions were set at 10 m and 40 m, respectively, as shown in Fig. 22(c) and (e). The corresponding MC results are presented in Fig. 22(c)-(f). The results show that, for the same platform, the z^{gt}/z_d values are nearly identical under thin Chl layers with different peak depths. Since the increase in multiple scattering caused by the thin Chl layer is limited, the deviation of z^{gt}/z_d from the statistical model (Eq. (33)) remains within 10 %.

When the Chl layer becomes thicker (FWHM of 20 m), as shown in Fig. 22(g), the corresponding MC results are presented in Fig. 22(g) and (h). For the ICESat-2 platform, where the r_s is relatively large, the thickened Chl layer significantly enhances multiple scattering, leading to a decrease in z^{gt}/z_d from 0.65 to 0.55—a reduction of approximately 15.4 %. In contrast, for the airborne platform, under the same IOP distribution, the smaller r_s limits the reception of multiple-scattered photons, resulting in a smaller decrease in z^{gt}/z_d from 0.85 to 0.75—a reduction of about 11.8 %. To further analysis the influence of vertical Chl distribution on z^{gt}/z_d, the vertically integrated chlorophyll concentration, Chl$_{sum}$, was calculated as defined by the following equation:

$$\mathrm{Chl}_{sum} = \int_0^{100} \mathrm{Chl}(z)dz. \tag{51}$$

The relationships between Chl$_{sum}$ and z^{gt}/z_d of ICESat-2 and Airborne 0.35 km platforms are shown in Fig. 22(i) and 22(j), respectively. The results reveal that as Chl$_{sum}$ increases, the discrepancy between time-based signals and real-depth signals becomes more pronounced. Specifically, 1/(z^{gt}/z_d) exhibits an approximately linear positive correlation with Chl$_{sum}$, which corresponds to an inverse relationship with z^{gt}/z_d. Moreover, for platforms with larger r_s, z^{gt}/z_d changes more rapidly with Chl$_{sum}$.

In summary, the vertical distribution of IOPs affects the magnitude of the discrepancy between time-based signals and real depth signals. When the vertical distribution of IOPs is non-uniform, the values of z^{gt}/z_d deviate from those derived by statistical models that assume vertically uniform IOPs, as expressed in Eq. (34). When stratification is pronounced, particularly with a significant increase in Chl$_{sum}$, the discrepancy becomes especially notable. In addition, this effect becomes more significant for platforms with larger r_s. Therefore, when applying statistical models, the actual vertical distribution of IOPs should be considered, such as through retrieval from ocean lidar backscattered signals (Chen et al., 2021; Churnside and Donaghay, 2009). Furthermore, even with the vertical distribution of IOPs available, quantitatively assessing their impact on discrepancies remains challenging and requires a comprehensive consideration of the influencing factors listed in Table 1.

6. Conclusions

The detection depth of lidar has long been a subject of significant interest. In comparison to previous studies, this article is the first to propose that the subsurface signals measured by ocean lidar (i.e., the time-based profile) do not correspond to the actual profile of photons penetrating the water (i.e., the real depth profile). Specifically, because of multiple scattering during laser transmit in the water, the actual signal measured by lidar—recorded based on the arrival time of backscattered photons, does not accurately represent the actual depth distribution of photons. The work investigates the differences between these profiles across six typical platforms. These discrepancies are characterized by the ratio of the lidar attenuation coefficients (K_z/K_t) and the ratio of detection depths (z^{gt}/z_d) between the two profiles.

For Case-1 water, assuming a vertically homogeneous water column and neglecting sea surface fluctuations, and under the Petzold SPF, the

results show that, both b and r_s jointly influence the differences between the two profiles. As b and r_s increase, K_z/K_t rises, while z^{gt}/z_d decreases. These trends indicate that the differences between the two profiles intensify, highlighting a greater discrepancy between the time-based and real depth profiles. Based on the analysis of MC simulation data, this work establishes statistical models for K_z/K_t and z^{gt}/z_d as functions of b and r_s, with a focus on Case 1 waters.

Specifically, for platforms with smaller r_s, such as shipborne and airborne 0.35 km, when Chl ranges from 0.01 to 10 mg/m^3, K_z/K_t values range from 1 and 3.5, while z^{gt}/z_d ranges from 1 to 0.3. For platforms with larger r_s, such as airborne 3 km, ICESat-2, and CALIPSO, the differences between the time-based and real depth profiles are more pronounced. In these cases, K_z/K_t ranges from 1 to 4.5, and z^{gt}/z_d ranges from 1 to 0.25. This indicates that with larger Chl, the real depth represents only 25 % of the depth estimated by the time-based depth profile.

For underwater lidar, due to its smaller r_s, the time-based depth profile closely approximates the real depth profile when Chl is less than 5 mg/m^3 and under the Case-1 conditions. Among the six platforms analyzed, only the backscattered signal from underwater lidar accurately represents the real depth distribution. This finding also highlights the potential of underwater lidar for calibrating the lidar backscattered signals from other platforms. Overall, when using time-based depth profiles to evaluate other parameters or assess lidar penetration depth, the effects of multiple scattering must be accounted for.

In addition, sensitivity analysis of the statistical model reveals that K_z/K_t and z^{gt}/z_d are more sensitive to variations in water optical parameter b than to changes in r_s. The study also investigates the effect of the absorption coefficient a on the statistical model in non-Case-1 waters (i.e., when a and b are not solely determined by Chl). The results show that when a increases while b remains constant, the photon penetration depth is limited, suppressing multiple scattering effects. As a result, both K_z/K_t and z^{gt}/z_d approach 1. In contrast, when a remains constant and b increases, enhanced multiple scattering leads to greater deviations of K_z/K_t and z^{gt}/z_d from 1, indicating a larger discrepancy between the time-based and real depth signals.

A systematic analysis of SPF effects reveals that SPFs with stronger forward scattering correspond to longer photon paths and deeper penetration depths. Under Chl of 0.10 mg/m^3 and 1.00 mg/m^3, the differences between K_z/K_t and z^{gt}/z_d and the statistical models in Eq. (33) and Eq. (34) remain below 10 % across different SPFs. Within the range of B_P at fixed values, Chl = 0–10 mg/m^3, and r_s = 0–100 m, the errors in K_z/K_t and z^{gt}/z_d for both Petzold and HG_1 remain within 10 %, demonstrating the applicability of the statistical models (Eq. (33) and Eq. (34)) under varying SPFs. Furthermore, analysis of sea surface roughness effects shows that while surface roughness affects the detected depth, its influence on the ratio z^{gt}/z_d is minimal. Under sea conditions with wind speed $U < 20$ m/s, the differences between K_z/K_t, z^{gt}/z_d, and the statistical models (Eq. (33) and Eq. (34)) remain below 10 %.

Finally, the study examines the impact of vertically inhomogeneous IOPs. Results indicate that $1/(z^{gt}/z_d)$ exhibit a linear relationship with the vertical integral of Chl. As Chl_{sum} increases, multiple scattering effects become stronger, and the deviation from the statistical models (Eq. (34)) increases accordingly.

Moreover, there are areas for improvement in this work, including deriving more comprehensive statistical models that account for additional influencing factors (such as the absorption coefficient a and the vertical distribution of IOPs), and experimentally validating the applicability of the derived statistical models. These aspects will be addressed in future research. Finally, this study enhances our understanding of ocean lidar backscattered signals and is significant for detecting seabed depth, terrain, and Chl in ocean lidar applications. Moreover, it establishes an important foundation for improving the accuracy and precision of ocean parameter inversion from ocean lidars, thereby expanding the role of lidar in biogeochemical research.

CRediT authorship contribution statement

Mingjia Shangguan: Writing – review & editing, Writing – original draft, Visualization, Validation, Supervision, Software, Project administration, Methodology, Investigation, Funding acquisition, Formal analysis, Data curation, Conceptualization. **Yirui Guo:** Writing – original draft, Visualization, Software, Methodology, Formal analysis, Data curation. **Zhuoyang Liao:** Software, Investigation, Formal analysis, Data curation. **Zhongping Lee:** Writing – review & editing, Writing – original draft, Methodology, Investigation, Formal analysis.

Declaration of competing interest

The authors declare that they have no known competing financial interests or personal relationships that could have appeared to influence the work reported in this paper.

Data availability

Data will be made available on request.

Acknowledgments

This work was supported by the National Natural Science Foundation of China (Grant No. 42476184), the Natural Science Foundation of Xiamen, China (Grant No. 3502Z202473033), the National Key Research and Development Program of China (Grant No. 2022YFB3901704), and the Fundamental Research Funds for the Central Universities (Grant No. 20720200107).

References

Abdallah, H., Bailly, J.S., Baghdadi, N.N., Saint-Geours, N., Fabre, F., 2012. Potential of space-borne LiDAR sensors for global bathymetry in coastal and inland waters. IEEE J. Selected Top. Appl.Earth Observations Remote Sensing. 6, 202–216.
Adkins, J.F., 2013. The role of deep ocean circulation in setting glacial climates. Paleoceanography 28, 539–561.
Amani, M., Moghimi, A., Mirmazloumi, S.M., Ranjgar, B., Ghorbanian, A., Ojaghi, S., Ebrahimy, H., et al., 2022. Ocean remote sensing techniques and applications: a review (part i). Water 14, 3400.
Bao, D., Wang, J., Hua, D., 2022. Investigation on inversion method of ocean salinity based on high spectra resolution lidar, eighth symposium on novel photoelectronic detection technology and applications. SPIE 2887–2897.
Barry, J.P., Widdicombe, S., Hall-Spencer, J.M., 2011. Effects of ocean acidification on marine biodiversity and ecosystem function. Ocean Acidification. 192–209.
Bissonnette, L.R., Roy, G., Roy, N., 2005. Multiple-scattering-based lidar retrieval: method and results of cloud probings. Appl. Opt. 44, 5565–5581.
Blondeau-Patissier, D., Gower, J.F., Dekker, A.G., Phinn, S.R., Brando, V.E., 2014. A review of ocean color remote sensing methods and statistical techniques for the detection, mapping and analysis of phytoplankton blooms in coastal and open oceans. Prog. Oceanogr. 123, 123–144.
Chen, P., Pan, D., 2019. Ocean optical profiling in South China Sea using airborne LiDAR. Remote Sens. Environ. 11, 1826.
Chen, P., Pan, D., Mao, Z., Liu, H., 2018. Semi-analytic Monte Carlo model for oceanographic lidar systems: lookup table method used for randomly choosing scattering angles. Appl. Sci. 9, 48.
Chen, G., Tang, J., Zhao, C., Wu, S., Yu, F., Ma, C., Xu, Y., et al., 2019a. Concept design of the "Guanlan" science mission: China's novel contribution to space oceanography. Front. Mar. Sci. 6, 194.
Chen, P., Pan, D., Mao, Z., Liu, H., 2019b. Semi-analytic Monte Carlo radiative transfer model of laser propagation in inhomogeneous sea water within subsurface plankton layer. Opt. Laser Technol. 111, 1–5.
Chen, P., Jamet, C., Mao, Z., Pan, D., 2020. OLE: A novel oceanic LiDAR emulator. IEEE Trans. Geosci. Remote Sens. 59, 9730–9744.
Chen, P., Jamet, C., Zhang, Z., He, Y., Mao, Z., Pan, D., Wang, T., et al., 2021. Vertical distribution of subsurface phytoplankton layer in South China Sea using airborne lidar. Remote Sens. Environ. 263, 112567.
Chen, X., Zhou, L., Zhou, M., Shao, A., Ren, K., Chen, Q., Gu, G., et al., 2022. Infrared ocean image simulation algorithm based on Pierson–Moskowitz spectrum and bidirectional reflectance distribution function. Photonics. MDPI 166.
Chen, S., Chen, P., Ding, L., Pan, D., 2023. A New semi-analytical MC model for oceanic LIDAR inelastic signals. Remote Sens. Environ. 15, 684.
Churnside, J.H., Donaghay, P.L., 2009. Thin scattering layers observed by airborne lidar. ICES J. Mar. Sci. 66, 778–789.

Churnside, J.H., Hunter, J.R., 1996. Laser remote sensing of epipelagic fishes, CIS selected papers: laser remote sensing of natural waters: from theory to practice. SPIE 38–53.
Churnside, J.H., Shaw, J.A., 2020. Lidar remote sensing of the aquatic environment. Appl. Opt. 59, C92–C99.
Churnside, J.H., Marchbanks, R., Lee, J.H., Shaw, J.A., Weidemann, A., Donaghay, P., 2012. Airborne lidar sensing of internal waves in a shallow fjord. Ocean Sens. Monitori. IV. SPIE 199–204.
Churnside, J.H., Wells, R., Boswell, K.M., Quinlan, J.A., Marchbanks, R.D., Mccarty, B.J., Sutton, T.T., 2017. Surveying the distribution and abundance of flying fishes and other epipelagics in the northern Gulf of Mexico using airborne lidar. Bull. Mar. Sci. 93, 591–609.
Churnside, J.H., Hair, J.W., Hostetler, C.A., Scarino, A.J., 2018. Ocean backscatter profiling using high-spectral-resolution lidar and a perturbation retrieval. Remote Sens. Environ. 10, 2003.
Collister, B.L., Zimmerman, R.C., Sukenik, C.I., Hill, V.J., Balch, W.M., 2018. Remote sensing of optical characteristics and particle distributions of the upper ocean using shipboard lidar. Remote Sens. Environ. 215, 85–96.
Collister, B., Hair, J., Hostetler, C., Cook, A., Ibrahim, A., Boss, E., Scarino, A.J., et al., 2024. Assessing the utility of high spectral resolution lidar for measuring particulate backscatter in the ocean and evaluating satellite ocean color retrievals. Remote Sens. Environ. 300, 113898.
D'alimonte, D., Liberti, G.L., Di Paolantonio, M., Kajiyama, T., Franco, N., Di Girolamo, P., Dionisi, D., 2024. In-water lidar simulations: the ALADIN ADM-Aeolus backscattered signal at 355 nm. Opt. Express 32, 22781–22803.
Eidam, E., Bisson, K., Wang, C., Walker, C., Gibbons, A., 2024. ICESat-2 and ocean particulates: a roadmap for calculating Kd from space-based lidar photon profiles. Remote Sens. Environ. 311, 114222.
Gao, W., Lv, Z., Dong, Y., He, W., 2006. A new approach to measure the ocean temperature using Brillouin lidar. Chin. Opt. Lett. 4, 428–431.
Gordon, H.R., 1982. Interpretation of airborne oceanic lidar: effects of multiple scattering. Appl. Opt. 21, 2996–3001.
Henyey, L.G., Greenstein, J.L., 1941. Diffuse radiation in the galaxy. Astrophys. J. 93, 70–83.
Hickman, G.D., Hogg, J.E., 1969. Application of an airborne pulsed laser for near shore bathymetric measurements. Remote Sens. Environ. 1, 47–58.
Hogan, R.J., 2006. Fast approximate calculation of multiply scattered lidar returns. Appl. Opt. 45, 5984–5992.
Hu, C., 2009. A novel ocean color index to detect floating algae in the global oceans. Remote Sens. Environ. 113, 2118–2129.
Jamet, C., Ibrahim, A., Ahmad, Z., Angelini, F., Babin, M., Behrenfeld, M.J., Boss, E., et al., 2019. Going beyond standard ocean color observations: lidar and polarimetry. Front. Mar. Sci. 6, 251.
Joint, I., Groom, S.B., Ecology, 2000. Estimation of phytoplankton production from space: current status and future potential of satellite remote sensing. J. Exp. Mar. Biol. 250, 233–255.
Kopilevich, Y.I., Surkov, A., 2008. Mathematical modeling of the input signals of oceanological lidars. J. Opt. Technol. 75, 321–326.
Lee, Z., Tang, J., 2022. The two faces of "Case-1" water. J. Rem. Sens. 2022, 9767452.
Lee, Z.P., Du, K.P., Arnone, R., 2005. A model for the diffuse attenuation coefficient of downwelling irradiance. J. Geophys. Res. Oceans 110.
Lee, Z., Wei, J., Voss, K., Lewis, M., Bricaud, A., Huot, Y., 2015. Hyperspectral absorption coefficient of "pure" seawater in the range of 350–550 nm inverted from remote sensing reflectance. Appl. Opt. 54, 546–558.
Li, X., Zhao, C., Ma, Y., Liu, Z., 2014. Field experiments of multi-channel oceanographic fluorescence lidar for oil spill and chlorophyll-a detection. J. Ocean Univ. China 13, 597–603.
Li, X., Chen, Y., Li, J., Jiang, J., Ni, Z., Liu, Z., 2016. Time-resolved fluorescence spectroscopy of oil spill detected by ocean lidar. In: Optical Measurement Technology and Instrumentation. SPIE, pp. 181–188.
Li, K., He, Y., Ma, J., Jiang, Z., Hou, C., Chen, W., Zhu, X., et al., 2020. A dual-wavelength ocean lidar for vertical profiling of oceanic backscatter and attenuation. Remote Sens. 12, 2844.
Li, C., Zhou, G., Zhang, D., 2024. Analysis of affecting factors for laser underwater transmission echo signals based on semi-analytic Monte Carlo. Int. J. Remote Sens. 45, 7185–7211.
Liao, Y., Shangguan, M., Yang, Z., Lin, Z., Wang, Y., Li, S., 2023. GPU-accelerated Monte Carlo simulation for a single-photon underwater lidar. Remote Sens. 15, 5245.
Lin, Z., Shangguan, M., Cao, F., Yang, Z., Qiu, Y., Weng, Z., 2023. Underwater single-photon lidar equipped with high-sampling-rate Multi-Channel data acquisition system. Remote Sens. Environ. 15, 5216.
Liu, D., Xu, P., Zhou, Y., Chen, W., Han, B., Zhu, X., He, Y., et al., 2019a. Lidar remote sensing of seawater optical properties: experiment and Monte Carlo simulation. IEEE Trans. Geosci. Remote Sens. 57, 9489–9498.
Liu, Q., Cui, X., Chen, W., Liu, C., Bai, J., Zhang, Y., Zhou, Y., et al., 2019b. A semianalytic Monte Carlo radiative transfer model for polarized oceanic lidar: experiment-based comparisons and multiple scattering effects analyses. J. Quant. Spectrosc. Radiat. Transf. 237, 106638.
Liu, Q., Cui, X., Jamet, C., Zhu, X., Mao, Z., Chen, P., Bai, J., et al., 2020. A semianalytic Monte Carlo simulator for spaceborne oceanic lidar: framework and preliminary results. Remote Sens. 12, 2820.
Maccarone, A., Drummond, K., Mccarthy, A., Steinlehner, U.K., Tachella, J., Garcia, D.A., Pawlikowska, A., et al., 2023. Submerged single-photon LiDAR imaging sensor used for real-time 3D scene reconstruction in scattering underwater environments. Opt. Express 31, 16690–16708.
Magalhaes, J., Da Silva, J., Batista, M., Gostiaux, L., Gerkema, T., New, A., Jeans, D., 2013. On the detectability of internal waves by an imaging lidar. Geophys. Res. Lett. 40, 3429–3434.
Mason, R.P., Sheu, G.R., 2002. Role of the ocean in the global mercury cycle. Glob. Biogeochem. Cycles 16, 40-41-40-14.
Mclean, J.W., Freeman, J.D., Walker, R.E., 1998. Beam spread function with time dispersion. Appl. Opt. 37, 4701–4711.
Mobley, C.D., Sundman, L.K., Boss, E., 2002. Phase function effects on oceanic light fields. Appl. Opt. 41, 1035–1050.
Moisan, J.R., Rousseaux, C.S., Stysley, P.R., Clarke, G.B., Poulios, D.P., 2024. Ocean temperature profiling lidar: analysis of technology and potential for Rapid Ocean observations. Remote Sens. 16, 1236.
Morel, A., 1974. Optical properties of pure water and pure seawater. In: Optical Aspects of Oceanography.
Morel, A., 1988. Optical modeling of the upper ocean in relation to its biogenous matter content (case I waters). J. Geophys. Res. Oceans 93, 10749–10768.
Mullen, L.J., Vieira, A.J., Herezfeld, P., Contarino, V.M., 1995. Application of RADAR technology to aerial LIDAR systems for enhancement of shallow underwater target detection. IEEE Transact. Microwave Theory Techniq. 43, 2370–2377.
Neumann, T.A., Martino, A.J., Markus, T., Bae, S., Bock, M.R., Brenner, A.C., Brunt, K.M., et al., 2019. The ice, cloud, and land elevation satellite–2 Mission: a global geolocated photon product derived from the advanced topographic laser altimeter system. Remote Sens. Environ. 233, 111325.
Parrish, C.E., Magruder, L.A., Neuenschwander, A.L., Forfinski-Sarkozi, N., Alonzo, M., Jasinski, M., 2019. Validation of ICESat-2 ATLAS bathymetry and analysis of ATLAS's bathymetric mapping performance. Remote Sens. 11, 1634.
Petzold, T.J., 1972. Volume Scattering Functions for Selected Ocean Waters.
Pierson Jr., W.J., Moskowitz, L., 1964. A proposed spectral form for fully developed wind seas based on the similarity theory of SA Kitaigorodskii. J. Geophys. Res. 69, 5181–5190.
Prieur, L., Sathyendranath, S., 1981. An optical classification of coastal and oceanic waters based on the specific spectral absorption curves of phytoplankton pigments, dissolved organic matter, and other particulate materials 1. Limnol. Oceanogr. 26, 671–689.
Rani, M., Masroor, M., Kumar, P., 2021. Remote sensing of ocean and coastal environment–overview. Remote Sens. Ocean Coastal Environ. 1–15.
Regnier, P., Resplandy, L., Najjar, R.G., Ciais, P., 2022. The land-to-ocean loops of the global carbon cycle. Nature 603, 401–410.
Samberg, A., 2005. Advanced oil pollution detection using an airborne hyperspectral lidar technology, laser radar technology and applications X. SPIE 308–317.
Shangguan, M., Weng, Z., Lin, Z., Lee, Z., Shangguan, M., Yang, Z., Sun, J., et al., 2023a. Day and night continuous high-resolution shallow-water depth detection with single-photon underwater lidar. Opt. Express 31, 43950–43962.
Shangguan, M., Yang, Z., Lin, Z., Lee, Z., Xia, H., Weng, Z., 2023b. Compact long-range single-photon underwater lidar with high spatial-temporal resolution. IEEE Geoscience Remote Sensing Letters. 20, 1–5.
Shangguan, M., Yang, Z., Shangguan, M., Lin, Z., Liao, Z., Guo, Y., Liu, C., 2023c. Remote sensing oil in water with an all-fiber underwater single-photon Raman lidar. Appl. Opt. 62, 5301–5305.
Shangguan, M., Guo, Y., Liao, Z., 2024a. Shipborne single-photon fluorescence oceanic lidar: instrumentation and inversion. Opt. Express 32, 10204–10218.
Shangguan, M., Liang, Y., Li, Y., Mo, Y., 2024b. Time-multiplexing single-photon imaging lidar with single-pixel detector. Appl. Phys. Lett. 124.
Shangguan, M., Liao, Z., Guo, Y., 2024c. Simultaneous sensing profiles of beam attenuation coefficient and volume scattering function at 180° using a single-photon underwater elastic-Raman lidar. Opt. Express 32, 8189–8204.
Shangguan, M., Yang, Z., Lin, Z., Weng, Z., Sun, J., 2024d. Full-day profiling of a beam attenuation coefficient using a single-photon underwater lidar with a large dynamic measurement range. Opt. Lett. 49, 626–629.
Shen, X., Kong, W., Chen, P., Chen, T., Huang, G., Shu, R., 2022. A shipborne photon-counting lidar for depth-resolved ocean observation. Remote Sens. 14, 3351.
Spence, D.J., Neimann, B.R., Pask, H.M., 2023. Monte Carlo modelling for elastic and Raman signals in oceanic LiDAR. Opt. Express 31, 12339–12348.
Spence, D., Kitzler, O., Taylor, C., Curtis, S., Neimann, B., Dawes, J., Downes, J., et al., 2024. Depth-resolved water temperature measurements using Raman LiDAR, 63, pp. 4366–4371.
Steinvall, O.K., Koppari, K.R., Karlsson, U.C., 1993. Experimental evaluation of an airborne depth-sounding lidar. Opt. Eng. 32, 1307–1321.
Trees, C.C., 2014. Beyond bathymetry: probing the ocean subsurface using ship-based lidars. Ocean Sensing and Monitoring VI. SPIE 188–197.
Walker, R.E., Mclean, J.W., 1999. Lidar equations for turbid media with pulse stretching. Appl. Opt. 38, 2384–2397.
Wang, Y., Zhang, J., Zheng, Y., Xu, Y., Xu, J., Jiao, J., Su, Y., et al., 2023. Brillouin scattering spectrum for liquid detection and applications in oceanography. Opto-Electron. Adv. 6, 220016.
Winker, D., Hostetler, C., Hunt, W., 2004. Caliop: the Calipso lidar, 22nd Internation laser radar conference (ILRC 2004), p. 941.
Wu, D., Chen, P., Kong, W., Pan, D., 2024. A novel semi-analytical method for Modeling polarized oceanic profiling lidar multiple scattering signals. IEEE Trans. Geosci. Remote Sens. 62, 3369099.
Yang, Y., Shangguan, M., 2023. Inversion of seawater temperature, salinity, and sound velocity based on Brillouin lidar. J. Mod. Opt. 70, 470–482.
Yu, Y., Ma, Y., Li, H., Huang, J., Fang, Y., Liang, K., Zhou, B., 2014. Simulation of simultaneously obtaining ocean temperature and salinity using dual-wavelength Brillouin lidar. Laser Phys. Lett. 11, 036001.

Yuan, D., Mao, Z., Chen, P., He, Y., Pan, D., 2022. Remote sensing of seawater optical properties and the subsurface phytoplankton layer in coastal waters using an airborne multiwavelength polarimetric ocean lidar. Opt. Express 30, 29564–29583.
Zege, E.P., Katsev, I.L., Prikhach, A.S., Ludbrook, G.D., Bruscaglioni, P., 2003. Analytical and computer modeling of oceanic lidar performance, 12th international workshop on lidar multiple scattering experiments. SPIE 189–199.
Zhang, X., Hu, L., 2009. Scattering by pure seawater at high salinity. Opt. Express 17, 12685–12691.
Zhou, Y., Chen, W., Cui, X., Malinka, A., Liu, Q., Han, B., Wang, X., et al., 2019. Validation of the analytical model of oceanic lidar returns: comparisons with Monte Carlo simulations and experimental results. Remote Sens. 11, 1870.
Zhou, G., Li, C., Zhang, D., Liu, D., Zhou, X., Zhan, J., 2021. Overview of underwater transmission characteristics of oceanic LiDAR. IEEE J. Selected Top. Applied Earth Observat. 14, 8144–8159.
Zhou, Y., Chen, Y., Zhao, H., Jamet, C., Dionisi, D., Chami, M., Di Girolamo, P., et al., 2022. Shipborne oceanic high-spectral-resolution lidar for accurate estimation of seawater depth-resolved optical properties. Light: Sci. Applicat. 11, 261.